IMAGING NEURAL CIRCUITS UNDERLYING LEARNING AND BEHAVIOR

by

JOSEPH B. WEKSELBLATT

A DISSERTATION

Presented to the Department of Biology
and the Graduate School of the University of Oregon
in partial fulfillment of the requirements
for the degree of
Doctor of Philosophy

December 2017

DISSERTATION APPROVAL PAGE

Student: Joseph B. Wekselblatt

Title: Imaging Neural Circuits Underlying Learning and Behavior

This dissertation has been accepted and approved in partial fulfillment of the requirements for the Doctor of Philosophy degree in the Department of Biology by:

Chris Doe	Chairperson
Cris Niell	Co-Advisor
Terry Takahashi	Co-Advisor
Mike Wehr	Core Member
Matt Smear	Institutional Representative

and

Sara D. Hodges	Interim Vice Provost and Dean of the Graduate School

Original approval signatures are on file with the University of Oregon Graduate School.

Degree awarded December 2017

DISSERTATION ABSTRACT

Joseph B. Wekselblatt

Doctor of Philosophy

Department of Biology

December 2017

Title: Imaging Neural Circuits Underlying Learning and Behavior

Sensory perception is context dependent and is likely modulated by task demands, learning and engagement to best serve specific goals of the organism. Sensory-driven behaviors also engage a cascade of cortical regions to process sensory input and generate motor output. To investigate the temporal dynamics of neural activity at this global scale, we have improved and integrated tools to perform functional imaging across large areas of cortex using a transgenic mouse expressing a fluorescent activity sensor. Imaging during an orientation discrimination task reveals a progression of activity in different cortical regions associated with different phases of the task. After cortex-wide patterns of activity are determined, we demonstrate the ability to select a region that displayed conspicuous responses for two-photon microscopy, and find that activity in populations of individual neurons in that region correlates with locomotion in trained mice.

We also found that learning a visual discrimination reduced population activity in visual cortex. To further investigate this phenomenon, we used two-photon microscopy to image mice before or after they had learned a visual discrimination. We find that excitatory neurons in layer 2/3 show striking diversity in their temporal dynamics during the behavior and classify them into transient, sustained, and suppressed groups. Notably, these groups exhibit different visual tuning and modulation by locomotion. The

functionally defined cell classes are also differentially modulated by training condition: showing both a cell class specific decrease in fraction responsive to visual stimuli after learning, and an increase in modulation by task engagement specific to trained animals. The characterization of pyramidal neuron subtypes in layer 2/3 of V1, and quantification of their distinct changes over learning, provides new insight into the circuit elements and pathways that enable goal-directed sensory processing.

This dissertation includes published and unpublished co-authored material. This dissertation also includes four supplemental movies related to functional imaging techniques described in chapter II.

CURRICULUM VITAE

NAME OF AUTHOR: Joseph B. Wekselblatt

GRADUATE AND UNDERGRADUATE SCHOOLS ATTENDED:

University of Oregon, Eugene, OR
Brown University, Providence, RI

DEGREES AWARDED:

Doctor of Philosophy, Biology, 2017, University of Oregon
Bachelor of Arts, Cognitive Science, 2008, Brown University

AREAS OF SPECIAL INTEREST:

Neurobiology
Sensory Physiology

PROFESSIONAL EXPERIENCE:

Graduate Research Fellow, Tory Herman Laboratory, University of Oregon, June 2012 – December 2017

Graduate Teaching Fellow, Department of Biology, University of Oregon, September 2011 – June 2012

Research Assistant, Brain Development Lab (Dr. Helen Neville), University of Oregon, July 2010 – September 2011

GRANTS, AWARDS, AND HONORS:

National Science Foundation (NSF) Graduate Research Fellowship Program, Honorable Mention recipient, 2013

National Institute of Health Developmental Biology Training Grant, University of Oregon, 2011-2014

UO Lewis Center for Neuro-Imaging (LCNI) Student Pilot Funds Award, "Visual streams of mice and men: Task-specific recruitment of brain regions for processing location and orientation," 2014

National Institute of Health Ruth L. Kirschstein National Research Service Award, "Task specific modulation of sensory signals in the mouse visual system," 2014 -2017

PUBLICATIONS:

Wekselblatt JB, Flister ED, Piscopo DM, Niell CM. Large-scale imaging of cortical dynamics during sensory perception and behavior. Journal of Neurophysiology. 115 (2016), pp. 2852–2866.

Wekselblatt JB, Niell CM. Behavior State – Getting "In The Zone." Neuron. (2015), 87(1): pp. 7-9.

Wekselblatt JB, Niell CM. Distinct functional classes of excitatory neurons are differentially modulated by learning and task engagement (To be submitted to eLife this month)

ACKNOWLEDGMENTS

I would like to thank my advisor, Cris Niell, who has been an outstanding mentor, friend, and confidant during my time in his lab. I would also like to extend thanks to all the members of the Niell lab, past and present, for their support and friendship. Additionally I would like to thank the members of my committee, Chris Doe, Terry Takahashi, Mike Wehr, and Matt Smear for providing me with valuable input and feedback through the years. This work was supported in part by a Pre-doctoral National Research Service Award, NIH Grant Number: 1F31EY025459-01A1, from the National Eye Institute, and by the University of Oregon Developmental Biology Training Grant, NIH Grant Number 5 T32 HD007348-23.

TABLE OF CONTENTS

LIST OF FIGURES

CHAPTER I

INTRODUCTION

The ability to focus cognitive resources on relevant information, while filtering or ignoring extraneous information, is a fundamental neural mechanism that is a precursor to many other cognitive functions. Performing many types of goal-directed behaviors, ranging from having a conversation on a busy street to locating a friend in a crowded room, depends directly on modulation of sensory processing based on the specific task demands. Learning to use a specific sensory modality, or specific stimulus features within a modality to perform a task, is known to influence the sensory representations, computations, and information flow within the brain. In the primate visual system, sensory modulation based on specific task demands is able to gate whether and how information is transmitted to the higher order visual areas specialized for processing relevant visual features. However, there is still much that is unknown about the role of the primary visual cortex and specific extrastriate visual areas in guiding behavior. Furthermore the neural mechanisms by which these areas are modulated according to task demands and task engagement are poorly understood. This is especially true in the mouse visual system, which has recently emerged as a dominant genetic model species for studying how sensory neocortex extracts cues to guide behavior in mammals.

This dissertation presents new methods for recording neural activity across many brain areas simultaneously, and describes the use of an unbiased approach to target specific areas that show functional significance for cellular resolution two-photon imaging. Calcium imaging provides the ability to record from large populations of

genetically identified neurons, providing many advantages over conventional electrical recording techniques. We present and characterize a new transgenic mouse line that expresses an ultra-sensitive genetically encoded calcium indicator, GCaMP6s, which has become very popular within the neuroscience community over the past couple of years (Burgess et al., 2017; Steinmetz et al., 2017; Wekselblatt et al., 2016). We use this mouse, in combination with the implantation of a chronic cranial window, and training of visual discrimination behaviors, to allow recording of neural activity over multiple scales.

In chapter II, we fully characterize the newly developed transgenic mouse expressing GCaMP6s in all cortical excitatory neurons as well as improve upon imaging techniques for investigating neural activity at both the widefield (activity across cortical areas) and two-photon levels (activity of individual neurons). We show the ability to monitor multiple brain areas simultaneously in animals while they perform complex visually guided behaviors, and correlate large-scale activity patterns with different phases of the task. We also show that this unbiased approach, and recordings over large areas of cortex, allows for the discovery of unexpected patterns of activity that can be further probed at single cell resolution using two-photon calcium imaging. Here, we identify a region in lateral occipital cortex whose activity is correlated with locomotor activity in trained mice, and term it the Lateral Occipital Locomotor Area (LOLA). This area shows populations of individual neurons that show locomotion locked responses. We find both populations that increase and decrease their activity with running in trained animals.

Chapter II contains previously published co-authored work. It is reproduced from the Journal of Neurophysiology (2016). Author contributions: Cristopher M. Niell conception and design of research; Joseph B. Wekselblatt and Denise M. Piscopo

performed experiments; Joseph B. Wekselblatt, Erik D. Flister, and Cristopher M. Niell analyzed data; Joseph B. Wekselblatt, Erik D. Flister, Denise M. Piscopo, and Cristopher M. Niell interpreted results of experiments; Joseph B. Wekselblatt, Erik D. Flister, Denise M. Piscopo, and Cristopher M. Niell prepared figures; Joseph B. Wekselblatt, Denise M. Piscopo, and Cristopher M. Niell drafted manuscript; Joseph B. Wekselblatt, Erik D. Flister, Denise M. Piscopo, and Cristopher M. Niell edited and revised manuscript; Joseph B. Wekselblatt, Erik D. Flister, Denise M. Piscopo, and Cristopher M. Niell approved final version of manuscript.

In Chapter III, we use the methods described in chapter II to investigate learning and task engagement related changes in primary visual cortex. This study was inspired, in part, by the observation that trained animals showed decreased population activity across visual cortex after being trained in the visual discrimination task described in chapter II. We felt this was an interesting and unexpected phenomenon as one might expect signals related to a discrimination to be enhanced over training. To investigate what was changing over learning we performed two-photon calcium imaging in targeted regions of primary visual cortex either before or after animals had learned a visual discrimination task. To control for effects due to repeated exposure to the stimuli used in the behavior, we also recorded from a group of animals who were experienced with the visual stimuli (to the same level as the trained animals) but had not learned a visual discrimination rule.

In the course of recording from an enormous number of neurons across the different behavior training conditions (>10,000), we discovered striking heterogeneity in the time-course of the responses of layer 2/3 excitatory neurons labeled by the CamKII

promoter. Using hierarchical clustering we were able to identify tree functionally distinct populations of neurons, which we term transient, sustained, and suppressed cell classes. Notably, we find that these cell classes display different selectivity for stimulus features and exhibit different levels of modulation by behavioral state. Furthermore, we show that there are cell class-specific changes in the proportion of active neurons after training and that the modulation due to task engagement is specifically enhanced for both transient and sustained cells after animals learn the visual discrimination task. Chapter III contains unpublished co-authored work, which was done in collaboration with my advisor Cristopher M. Niell.

This characterization of heterogeneity in the layer 2/3 excitatory population, as well as the quantification of cell-type specific changes over learning and task engagement provide an important refinement on how we understand the neural mechanisms by which context dependent processing is carried out by the brain. We expect the methods described here, in chapter II, and used in chapter III to investigate learning, will be useful to probe information flow and network processing in brain-wide circuits involved in many sensory and cognitive processes.

CHAPTER II

LARGE-SCALE IMAGING OF CORTICAL DYNAMICS DURING SENSORY PERCEPTION AND BEHAVIOR

Introduction

One of the central challenges in neuroscience is to understand how sensory input is processed and used to guide behavior. This involves the flow of neural activity and transformation of encoded information across multiple brain regions. In vision (Felleman and Van Essen 1991), these include primary visual cortex and extrastriate regions to extract information from the visual scene, higher-order association areas involved in decision-making, and motor regions to generate appropriate behavior.

Electrophysiological studies of single unit activity underlying sensory-driven behavior have generally been limited to recording either one or a small number of regions at a time. For example, one may target primary visual cortex in studying sensory encoding, or frontal cortical areas for decision-making. In addition to limiting the understanding of temporal dynamics and interactions across areas, such an approach makes it likely that one might miss a previously unknown region that might be involved in processing, due to the infeasibility of simultaneously recording individual neurons across the expanse of cortex with electrodes.

Recently, imaging methods have been developed for species with smaller nervous systems, including nematodes and zebrafish larvae, to allow imaging of activity across nearly complete neural populations (Ahrens et al. 2012; Prevedel et al. 2014). However, these species lack cortex. At the other end of the complexity spectrum, functional imaging and EEG methods in humans allow approximate localization of task-specific activity to cortical areas, but lack high spatial resolution and the capacity for follow-up causal studies that are available in genetic model systems.

Here we present a toolbox of methods to bridge these domains in the mouse, using widefield imaging to measure dynamic patterns of activity across broad regions of cortex during behavior, then targeting areas of interest for two-photon imaging. The mouse is a prime model system for understanding cortical circuits due to the genetic tools available (Luo et al. 2008; O'Connor et al. 2009), as well as the development of behavioral paradigms to probe sensory and cognitive function (Carandini and Churchland 2013). While recent studies have used both intrinsic signal imaging and GCaMP3 to generate static maps of sensory topography in the mouse (Andermann et al. 2011; Issa et al. 2014; Marshel et al. 2011; Tohmi et al. 2014), these methods have not shown the sensitivity and temporal resolution necessary to track activity at the timescale of behavior.

We achieve this goal using a new transgenic mouse line, which expresses the fluorescent calcium indicator GCaMP6s in excitatory neurons throughout cortex under the control of a tTA driver line. GCaMP6s is an ultra-sensitive indicator of neuronal activity (Chen et al. 2013) that allows detection of single action potentials in individual neurons with two-photon imaging. Using a transgenic line allows broad expression of the

indicator and provides a global view of cortical activity. By imaging GCaMP6s mice with widefield tandem-lens optics similar to that used in intrinsic imaging (Ratzlaff and Grinvald 1991), we observe activity across the dorsal surface of cortex with adequate signal-to-noise and spatio-temporal resolution to track local activation during single trials within many cortical areas simultaneously at the timescale of behavioral events.

We demonstrate the utility of this method by 1) mapping multiple sensory/motor modalities across the cortical surface, 2) rapidly generating maps of extrastriate visual areas, which can be aligned across sessions and subjects, 3) imaging the dynamics of activity across cortical areas during the performance of a visual discrimination task, and 4) performing targeted two-photon imaging to measure the response properties of ensembles of neurons within functionally localized regions, including an association area between visual, somatosensory, and auditory cortex that was identified in the behavioral task. Thus, using a combination of widefield and targeted two-photon imaging, we are able to span the scale of the brain from global patterns of activity across multiple areas, down to cellular resolution in local networks.

Methods

DNA Constructs

Plasmid encoding the DNA sequence for GCaMP6s (pGP-*syn*-GCaMP-nls-mCherry-WPRE) was obtained from D. Kim (Janelia Farm). To generate the tetO-GCaMP6s transgenic mouse, the coding sequences for GCaMP6s-nls-mCherry-WPRE were subcloned into a pTRE-tight plasmid (Clontech), placing GCaMP6s expression

under the control of the tetracycline response element (TRE; tetO). All constructs were verified by sequencing.

Transgenic Mice

Animals were maintained in the animal facility at University of Oregon and used in accordance with protocols approved by the University of Oregon Institutional Animal Care and Use Committee. tetO-GCaMP6s mice were generated by injection of a gel-purified linear DNA fragment into fertilized oocytes. Embryos for injection were obtained by mating (C57BL/6J and CBA) F1 hybrids. Transgenic founders were crossed to mice expressing tTA under the control of the CaMK2a promoter on the C57BL/6J background (JAX stock number 007004). Primers for genotyping are 5'-GGGATCTGTACGACGATGACG-3' (forward) and 5'-CTCGATGTTGTGGCGGATGT-3' (reverse). This mouse strain has been deposited at The Jackson Laboratory (stock number 024742).

Although our expression construct included a nuclear-localized mCherry reporter, we did not detect noticeable red fluorescence in cortex, perhaps due to poor IRES-mediated downstream gene expression. However, lack of a co-label did not impact the methods described here.

Histology

Animals were euthanized under deep anesthesia by cervical dislocation. Animals were either perfused (for ISH) or the brain was removed immediately and fixed by immersion in 4% paraformaldehyde in PBS at 4°C overnight, after which 30-70um coronal sections were cut with a vibratome. The sections were mounted using

Vectashield with DAPI (Vector Laboratories) and imaged on a Zeiss AxioImager A2 microscope with 2X and 20X air objectives.

Co-localization of CaMKII and GCaMP6 expression by nonradioactive ISH was performed as described previously (Wehr et al. 2009). For GCaMP6, we used a digoxygenin (DIG)-labeled pWPRE riboprobe (1:500), visualized by anti-digoxygenin sheep Fab fragments conjugated to horseradish peroxidase (Roche No. 11207733907). For CaMKII, we used a FITC- riboprobe (1:1000). Following overnight incubation at room temperature, 30µm thaw-mounted sections were washed at room temperature with MABT buffer 5 × 5', and then AP staining buffer 2 × 10', after which 3.5µl/ml NBT and 2.6µl/ml BCIP, and 80µl/ml levamisole were added and the colorimetric reaction was allowed to develop for 3 hours at 37°C under agitation. The reaction was stopped by two washes with PBS (0.1% Tween-20), then two washes in DI H_2O.

Animal use

All procedures were conducted in accordance with the ethical guidelines of the National Institutes of Health and were approved by the IACUC at University of Oregon. Adult mice 2–8 months old, both male and female, were used in this study. Animals were maintained on a 12hr light / 12hr dark reverse light cycle. Training and experiments were performed during the dark phase of the cycle.

The spherical treadmill was based on Dombeck et al (2007) and Niell and Stryker (2010), with modifications by L. Fischer (mousevr.blogspot.com). Briefly, Tygon E-3603 tubing supplied pressurized air through the bottom of a hollow polystyrene hemisphere (OD 250mm, ID 200mm) (Graham Sweet studios). A 200mm hollow polystyrene ball

placed inside the hemisphere provided a freely rotating surface on which the mouse stood. Air flow was set to just enough to allow free rotation using a rotameter with valve (mcmaster.com 41945K77) connected with a hose fitting (mcmaster.com 5346K18). This configuration significantly reduced noise relative to previous implementations, especially by also replacing standard lab air nozzles/valves with large diameter hose fittings (mcmaster.com 5346K19) and valves (mcmaster.com 4082T43) set to fully open. The animal's head was fixed via a surgically attached headplate that could be screwed into a rigid crossbar above the floating ball. Headplates were manufactured from titanium for biocompatibility, by emachineshop.com. Designs are available upon request.

Surgical Procedures

The cranial window implant procedure was based on Holtmaat et al. (2009) with modifications as described below. First, a titanium headplate was cemented to the skull to allow head fixation. Animals were anesthetized using isoflurane (3% induction; 1.5%–2% maintenance), in 100% O2 (0.8 – 1.0 L/min), and positioned in a stereotax using earbars placed just below the ear canal for stability. The animals were given subcutaneous injections of the analgesic carprofen (5mg/kg) and 0.2ml saline to prevent post-operative dehydration. Body temperature was maintained at 37.5°C by a feedback-controlled heating pad; temperature and breathing were monitored throughout surgery. Sterilized instruments and aseptic technique were used throughout. Sterile ocular lubricant (Puralube) was applied at the beginning of each surgical procedure. Scalp hair was removed using an electric shaver, and the surgical site was cleaned using 70% isopropanol applied with cotton tip applicators. Topical lidocaine hydrochloride jelly (2%, Akorn) was applied and left for 1-2 minutes before being cleared with isopropanol.

Betadine was then applied to surgical site with cotton tipped applicators for final sterilization.

Following a scalp incision, the periosteum was cleared from the surface of the skull using #5 forceps. Once the skull was completely cleared of connective tissue, sutures were marked using a surgical skin marker (Securline), along with the center position for window implantation (3.5mm lateral, 1.5mm anterior of Bregma for visual cortex). Next, the surface of the skull was lightly scored and a thin layer of cyanoacrylate (VetBond, WPI Inc.) was applied, to provide a substrate to which the dental acrylic could adhere. The headplate was then attached to the skull with black (for light block) dental acrylic (Ortho-jet) and the opening in the headplate was filled with a silicone elastomer (Kwik-Sil, WPI Inc.) to protect the skull. The animal was allowed to recover for several days with free access to food and water before subsequent cranial window surgery.

Following recovery from the headplate surgery, a 5-8mm diameter cranial window (No. 1 coverglass, Warner Insturments) was implanted. Surgical preparation was as above, with the addition of dexamethasone sodium phosphate (2 mg/kg subcutaneously) ~3 hr prior to surgery to reduce brain edema. The anesthetized animal was stabilized by screwing the headplate to a custom machined fork. The silicone plug was removed from the well of the headplate and the skull was cleaned with isopropanol and rinsed with saline. A craniotomy matching the diameter of the window was made with a pneumatic dental drill (Western Tradition) with carbide burs (FG 1/4). To prevent heating of cortex, the drilling of the craniotomy was done slowly, using compressed air to blow off bone chips with a cold sterile saline rinse between short periods of drilling. When drilling across the sutures, care was taken to avoid damaging the underlying

sinuses. Once the inner portion of the craniotomy moved somewhat freely when touched, angled forceps were used to carefully remove the center piece of bone, lifting vertically while the skull was immersed in saline.

A thin layer of transparent polymer (part no. 3-4680, Dow Corning), used to seal craniotomies in primates (Jackson and Muthuswamy 2008), was applied to the dura surface, just enough to cover the craniotomy, for protection and stability. The coverslip was secured in place using cyanoacrylate applied around the edges of the window followed by dental acrylic. Because the polymer fills the gap between the curved cortical surface and the coverslip, the cortex was not flattened by pressing the coverslip against it. The mice were allowed to recover for at least 4 days before beginning habituation and training.

Imaging

Our custom macroscope was based on the tandem lens design used for intrinsic signal imaging (Kalatsky and Stryker 2003; Ratzlaff and Grinvald 1991). Two camera lenses (Nikon 50mm f/1.2 and 105mm f/1.8) were interfaced with a dichroic filter cube (Thorlabs). Blue and green illumination were provided by LEDs (Luxeon Rebel 470nm 70lm and 530nm 161lm) with custom driver hardware using feedback stabilization to control light levels to <0.1% variability during rapid switching, since LEDs are subject to fast current-temperature-brightness dynamics. Blue light illumination was supplied in epifluorescence configuration through the filter cube housing a HQ470/40x excitation filter, T495lpxr dichroic mirror, and HQ525/50m emission filter (Chroma Technology). Green light was supplied directly through a fiber placed obliquely above the brain. The total power of blue light delivered to the specimen was 5-10mW, and because this is

spread over a large area it results in illumination intensity less than 0.1mW/mm^2. At these levels we did not observe bleaching over imaging sessions of multiple hours.

Green fluorescence or reflected light was collected and passed through the filter cube, then focused onto a pco.edge sCMOS detector (PCO Corporation). Images were acquired at 10Hz with 4x spatial binning using Camware software (PCO Corporation), with frame acquisition and LED illumination triggered by TTL pulses from the stimulus presentation computer to synchronize with visual stimulus frames. Illumination intensity, exposure duration, and data storage rate should be balanced to achieve high framerates and fill the dynamic range of the sensor.

Camera lenses allow a relatively high numerical aperture (NA) for light collection, which can also be adjusted easily using the f-stop setting in order to restrict the NA. This permits a flexible trade-off between sensitivity and depth of field, especially as increased depth of field is useful given the curvature of the cortical surface. Imaging was generally performed at an f-stop of 5.6. The ratio of the focal lengths of the two lenses determines image magnification. To map 1cm of cortex across the 2cm detector (6.5um pixels), we chose 50mm and 105mm lenses, yielding magnification of 2.1x and 3.1um specimen pixels. In practice, we find an effective spatial resolution of ~25um, based on the highest spatial frequencies present in non-binned images of vascular structure. Binning across spatially oversampled pixels can reduce shot noise by allowing more total photons to be detected with increased illumination or NA. This is a standard practice in intrinsic signal imaging (Kalatsky and Stryker 2003) and is generally applicable at high light levels where readout noise is negligible compared to photon count noise.

Two-photon imaging was performed using a MOM moveable objective microscope (Sutter Instruments, Inc.) coupled to a Mai-Tai HP Ti-Sapph pulsed laser, with a 16x/0.8NA objective (Nikon). ScanImage software (Pologruto et al. 2003) in Matlab was used for data acquisition, with a custom user function to record TTL output from the stimulus/behavior system on the imaging timebase for later synchronization. Images were acquired at 3.7fps and 256x256 pixels over a ~400x400um field of view, using 35-50mW illumination power as measured at the front aperture of the objective.

Stimulus delivery and behavior control

Visual stimuli were presented on a Viewsonic VA2342 LCD monitor (28 x 50cm, linearized by eye to correct for gamma (mean luminance 35cd/m^2), oriented tangentially 25 cm from the mouse's right eye (see Wiesenfeld and Branchek (1976) for optimal distance in rat vision) in portrait configuration, covering ~60x90° of visual space. Stimuli were generated with custom software using the Psychtoolbox extension for Matlab (Brainard 1997; Pelli 1997). For passive mapping of visual responses, we binarized a 1/f noise stimulus described previously (Niell and Stryker 2008) with spatial frequency corner of 0.05cpd and cutoff of 0.12cpd, and temporal frequency cutoff of 5Hz. This stimulus was binarized to black/white instead of grayscale to increase contrast and generate edges. Note that the hard edges imposed by binarization caused higher spatial frequency overtones.

For mapping of total visual responsiveness, this noise stimulus was presented in blocks of 5secs, with 5secs of gray screen intervening. For retinotopic mapping, this noise stimulus was masked to create a 20deg wide bar that moved across the visual display with a 10sec period (topographic noise stimulus, Figure 4A). In order to define

auditory responsive regions, white noise bursts of 50ms duration were presented at 2Hz (450msec inter-stimulus interval) for 5 sec, followed by 5 sec of silence.

Movement of the mouse on the spherical treadmill was measured with a single optical USB computer mouse positioned on the Styrofoam ball, acquired once per stimulus frame (60Hz) in Matlab. Note that because we only used one USB computer mouse to measure locomotion, we do not completely specify the motion of the ball. In order to maintain sensitivity to forward locomotion while maximizing sensitivity to lateral motion (used for behavioral response) the optical mouse was positioned laterally to the subject, midway between the vertical and horizontal axes. Therefore, one coordinate of the mouse's readout represents direct lateral movement of the subject, and the other coordinate represents a mixing of forward locomotion and rotation around the vertical axis. Therefore, while we can detect forward locomotion (moving vs stationary), there is a scale factor in the absolute speed of forward motion, which could be computed based on precise geometry but was not necessary for the current study.

The behavioral control system was based on Meier et al. (2011) with modifications to allow optical mouse input for behavioral report of responses and TTL control of the LEDs and sCMOS camera exposures. Visual stimuli for behavior consisted of 45° diameter circular patches of square wave gratings at random spatial phase with spatial frequency 0.16cpd. Visual stimuli for two-photon assessment of orientation selectivity consisted of full-display drifting square wave gratings of eight evenly-spaced directions of motion, at 2Hz temporal frequency and both 0.02cpd and 0.08cpd spatial frequency. These were presented in randomly interleaved order, along with a gray (linearized mean luminance) blank stimulus, for 4sec, with 4sec gray inter-stimulus

interval.

Behavioral training

Prior to beginning behavior, mice were handled for several days until they were comfortable with the experimenter. Once water scheduling was begun, animals received water only during and immediately after head-fixed training on the ball. Training sessions increased in duration over the course of 1–2 weeks, from 20 minutes to 2 hours per day.

All training was performed with a mostly automated system (Meier et al. 2011). First, mice learned the simple visual task of discriminating the location of a luminance stimulus. Animals were required to request a trial by stopping spontaneous locomotion for 1 second to receive a water reward. Upon requesting a trial, a stimulus was presented with dark on either the top or bottom 2/3 of the screen, and light on the other 1/3. The animal was rewarded with a second water drop for moving right (left) on the ball if dark was on the top (bottom). When an animal could reliably request trials, the water reward for stopping to initiate trials was eliminated. This task took about one week to learn and established trial structure and attention to the visual stimulus.

Once a mouse could perform a significant number of trials and reached ~75% accuracy on the luminance task, they were graduated to the orientation discrimination task. This task followed a similar structure, but a circular grating patch (either horizontal or vertical) was presented in the middle of the screen and the mouse was rewarded for moving left (right) for horizontal (vertical). The stimulus remained on the screen for one second after correct responses. Incorrect responses triggered a 3.5sec timeout with potentially aversive flashing error stimulus and 50% probability of a correction trial, where the previous stimulus was repeated until answered correctly, to prevent

development of a side bias.

During training, water rewards were calibrated by the experimenter to maintain consistent weights (>80% of baseline), corresponding to ~1.5ml of water through the course of a session. Mice were trained 7 days per week for 1-2 hours per day, with a session ending when the subject stopped initiating trials. We found that it was important to avoid letting the animals continue for extended periods after satiation, as this reduces motivation and slows training progress.

Imaging during behavior was performed after an animal reliably performed the orientation discrimination at >80% correct. The imaging behavioral configuration was identical to training, except the stimulus remained on the screen for one second even after incorrect responses, replacing the flashing error stimulus used during training, to avoid differences in visual input between correct and error trials.

Data analysis – widefield imaging

To analyze widefield images, 3:1 alternating blue and green frames were separately interpolated to produce a continuous image series at 10Hz. To account for differences across pixels in expression, illumination, and detection, following standard practice the fractional fluorescence change (dF/F) relative to the mean over the recording period (an approximation of the baseline) was calculated for each pixel in each channel. The apparent baseline showed some non-stationarity, including a decrease over the first few seconds after stimulus onset, likely due to adaptation. If such effects have spatial structure, such as being specific to visual areas, they could potentially distort phase maps, but in our data these non-stationarities were much smaller than visually evoked signals.

The green reflectance image was used to normalize the fluorescence image to compensate for changes in absorbance due to hemodynamics. This can be performed by dividing the normalized total signals (F/Fmean) or approximated by subtracting the fractional changes (dF/Fmean). Division of total signals and subtraction of fractional fluorescence are mathematically identical to first order in the Taylor expansion, and give experimentally indistinguishable results. Note that because signals at each pixel are normalized to Fmean, this correction does not depend on constant illumination across the field of view.

Temporal deconvolution was performed using the Lucy-Richardson non-negative deconvolution function in Matlab, using a bi-exponential convolution function with 180msec rise time and 550msec decay time, based on measured values (Chen et al. 2013). More advanced models of the mapping between neural activity and fluorescence changes could further improve deconvolution (Vogelstein et al. 2009). All widefield data presented was deconvolved except where noted in several examples comparing raw and deconvolved timecourses.

For analysis of block stimuli (Figures 2 and 4), we computed the mean dF/F during stimulus periods minus the mean dF/F during non-stimulus periods to obtain the stimulus-evoked response. For periodic stimuli (Figure 5), we computed the amplitude and phase of the Fourier component of the dF/F signal at the stimulus frequency (0.1Hz). Periodic mapping was also performed immediately before behavioral sessions to allow spatial registration in subsequent analyses.

To generate retinotopic maps from periodic stimuli, we computed the spatial gradient of the phase value for both azimuth and elevation maps, giving the Jacobian, a 4-

dimensional measure of relative topography at each cortical location (abstracting the absolute retinotopic location of the stimulus, which can vary between sessions and individuals). The azimuth and elevation components of the Jacobian were individually normalized to unit length, to avoid over-weighting pixels with artifactually large gradients, such as poorly responsive regions or craniotomy boundaries. The 4-dimensional representation was aligned across imaging sessions (x-y translation and rotation) by maximization of their cross-correlation. While the full 4-dimensional gradient completely describes the topography, it may also be possible to use the visual field sign alone to perform alignment.

To the extent that a given area's retinotopy is not highly warped, the azimuth and elevation gradients are roughly orthogonal and equal magnitude, which implies its topography can be summarized by a single angle of orientation and a single binary chirality (excluding within-map variations in "cortical magnification"). Chirality can be quantified by the "visual field sign" (Sereno et al. 1994), defined as the sine of the angle between the azimuth and elevation gradients, equivalent to the z-component of the cross-product between unit vectors along the gradients of the two maps. It is therefore a binary (for orthogonal components) function of the Jacobian whose sign indicates mirror reflected topography. It does not preserve information within region interiors, eliminating both sensitivity to potentially differential "cortical magnification" within regions and the opportunity for non-rigid within-region alignment across subjects or development.

Two methods were used for determining boundaries between retinotopic regions. In an automated partitioning approach (Fig 5E), we use a watershed transform of retinotopic position, supplemented by visual field sign boundaries. The zero contour of

visual field sign identifies most region boundaries, but misses those across saddle points such as between V1 and AM. We therefore performed a watershed transform of the retinotopic distance from the centroid of locations represented by the 30% most responsive pixels, followed by hmin smoothing of 1.22% of the standard deviation of distances, which delineated most region boundaries, including those that visual field sign missed. To generate a final partitioning, we took the union of the watershed and visual field sign boundaries and labeled areas that corresponded to published extrastriate maps. We note that using a lower hmin smoothing factor allowed all known boundaries to be identified without using visual sign, but led to additional subdivision within regions.

Alternately, distinct retinotopic areas were delineated for presentation by mapping the visual field sign and one axis of the azimuth gradient into RGB space. Regions where the visual field sign was negative were labeled red, and positive were labeled green. Because this does not unambiguously describe the local gradient, we also mapped the sign of the x-component of the azimuth gradient into the blue channel. Finally, the absolute amplitude of the local gradient was mapped into saturation of the RGB signal, so that regions with minimal gradient, representing poor topography, appeared white.

Behavioral data was analyzed by aligning imaging frames to stimulus onset, and computing the median dF/F across trials at each timepoint. The resulting average timecourse was then temporally deconvolved as described above. Performing deconvolution prior to averaging gives nearly identical results, but is far more computationally demanding.

Data analysis – two-photon imaging

Two-photon image data was first spatially aligned, using phase correlation to estimate x-y translation (courtesy of D. Ringach). Similar results could be obtained using imregcorr in Matlab. Cell body ROIs were extracted semi-automatically, by first manually selecting a pixel in the cell body from the mean fluorescence image and then automatically extracting all pixels within a 20um window that had >0.8 correlation coefficient in fluorescence timecourse with the selected pixel. This provided a clear outline of the cell body in nearly all locations selected that corresponded to a labeled neuron in the fluorescence images. The final signal for each cell was computed by taking the median dF/F timecourse across selected pixels, although this doesn't account for differences in SNR across pixels. Neuropil fluorescence was computed by extracting the mean dF/F in a region around the cell, with identified cell bodies removed. This signal was multiplied by a correction factor (ranging from 0.6 to 0.9) based on the fluorescence intensity in blood vessels, and subtracted from the cellular dF/F to give the corrected timecourse of activity. Deconvolution was not applied to two-photon data.

For analysis of drifting gratings, the mean dF/F during the second half of the preceding inter-stimulus interval was subtracted from the mean dF/F during stimulus presentation, to compute the evoked response. Visually responsive units were defined as those with a significantly different response to at least one grating stimulus relative to the gray blank condition (students t-test, $p<0.05$ with correction for multiple comparisons). Although this is a standard measure, response distributions are not Gaussian, violating the preconditions for Student's t-test; the lower power Komolgorov-Smirnof may be more appropriate for future studies. Orientation tuning curves were computed at the spatial

frequency that gave the strongest response for each cell, by computing the mean over the seven repeated presentations of each stimulus condition. The orientation selectivity index (OSI) was computed from the tuning curve as in Niell and Stryker (2008) and Chen et al (2013) as $(R_{pref}-R_{orth}) / (R_{pref}+R_{orth})$, from a fit to a sum of two wrapped Gaussians. Pixel-wise maps of orientation selectivity were computed in a similar manner, but based on the fluorescence trace at each pixel rather than summed over cell body ROIs.

Analysis of responses to locomotion was performed by first calculating the fractional fluorescence change for each cell (or individual pixel for pixel-wise maps) as described above, and then calculating the correlation coefficient between the fluorescence trace and running speed as measured by the optical mouse. Direct observation ruled out the possibility that low speeds corresponded to locomotion around the axis to which our single optical mouse was insensitive. Statistical significance was determined by comparing the measured correlation coefficient with the distribution of correlation coefficients computed for all possible temporal shifts. Units with a z-score of >2.6 (corresponding to $p<0.01$) relative to the shuffled distribution were considered significant. Data was pooled across the subjects, disregarding potential correlations of neurons within subjects. Although this is typically ignored, it may be significant when neural activity is largely influenced by subject-specific factors, as in spontaneous locomotion.

Unless otherwise noted, summary statistics are presented as medians with error bars representing bootstrapped confidence intervals.

Results

A transgenic mouse expressing an ultra-sensitive reporter of neural activity throughout cortex

With the goal of obtaining robust expression of GCaMP6s across the cortical surface, we generated a transgenic mouse expressing GCaMP6s under the control of a tetracycline-responsive promoter element (TRE; tetO). (Fig 1A). Following confirmation of transgene incorporation by PCR, we screened for GCaMP6s expression after crossing to a CaMK2-tTA driver line (Mayford et al. 1996). CaMK2 is expressed in most cortical excitatory cells, but not inhibitory GABAergic cells (Benson et al. 1992). In one founder line, we found strong expression throughout cortex, with a distribution that approximates the expression of the tTA driver. No fluorescence was observed in mice that were not crossed to the tTA driver line, confirming that expression is dependent upon the driver.

Expression was found across the extent of cortex, in a large fraction of cells in all cortical layers (Fig 1 B-D). *In situ* mRNA hybridization showed that GCaMP6s was co-expressed in most CaMK2-positive neurons (212/247 cells, 86 +/- 4% s.d., across three cortical locations). Furthermore, cells that expressed GCaMP6s always expressed CaMK2 indicating that expression is in excitatory neurons, consistent with the driver. The reliability of co-expression suggests that the observed variability in label density across cortical layers reflects the density of CaMK2-positive neurons. Importantly, we did not find evidence of fluorescence filling neuronal nuclei (Fig 1E), which has previously been correlated with cellular toxicity resulting from GCaMP over-expression (Tian et al. 2009). Although our expression construct included a nuclear-localized

mCherry reporter, we did not detect red fluorescence above wild-type background, perhaps due to poor IRES-mediated downstream gene expression.

Widefield mapping of neural activity across the dorsal surface of cortex

In order to image fluorescence signals across broad regions of cortex with adequate spatial and temporal resolution to isolate region-specific activation during behavior, we implemented a widefield epifluorescence system based on the tandem lens configuration commonly used for intrinsic signal imaging (Ratzlaff and Grinvald 1991). This consists of two 35mm camera lenses with an epifluorescence filter cube in between, projecting onto an sCMOS camera detector (Figure 2A). To image brain regions over multiple sessions, we implanted a metal headplate for head-fixation and performed a craniotomy up to 8mm in diameter, covered with a transparent polymer and a glass coverslip, to create a chronic cranial window. Ideal surgical outcomes result in a window that remains viable for 6 months or more. Head-fixed animals were placed on a spherical treadmill allowing locomotor behavior during imaging (Dombeck et al. 2007).

Illumination of cortex with blue light, in the transgenic GCaMP6s mouse line, results in bright fluorescence across the cortical surface (Fig 2B). In order to assess visual responses across areas of potentially dissimilar sensitivities, we presented binary spatiotemporal noise approximately distributed over the sensitivity range of reported mouse visual cortical areas (Marshel et al. 2011; Niell and Stryker 2008), which appears as full contrast moving edges (Movie S1 inset). To maximize responses, this was presented as a periodic stimulus (5 sec on, 5 sec off).

Since blood absorbs light though a wide band including the GCaMP excitation (blue) and fluorescence emission (green) wavelengths, changes in blood volume

significantly distort single photon *in vivo* GCaMP measurements (Fig 3B,E). This effect needs to be corrected, as it is much larger and less directly coupled to local neural activity than the intrinsic signal under red illumination, which arises from changes in hemoglobin oxygenation. Cortical reflectance in the green wavelengths that do not excite GCaMP provides a relatively isolated measure of the fraction of signal lost to hemodynamic absorbance. Normalizing the blue signal to this amount provides an estimate of the corrected fluorescence signal.

To perform the correction, on every 4^{th} frame we interleaved an image acquired with green, rather than blue illumination. Compared to the mixed signal under blue illumination, the green signal varies more slowly, with more delay from stimulus onset, and is strongest around vasculature (Fig 3A,D; B,E), where it approaches the scale of fractional change in GCaMP fluorescence under blue illumination.

We computed the corrected signal based on interpolated fractional changes, giving a result that was closely locked to the visual stimulus (Fig 2C,D, green). Finally, temporal deconvolution using the empirically measured GCaMP6s time constants (Chen et al. 2013) provided even greater temporal resolution (Fig 2D, black) and a close match to the temporal pattern of multi-unit neural activity recorded in V1 (figure 2D, blue).

Although the green reflectance subtraction cannot provide a complete correction, particularly since hemoglobin absorbance is slightly higher for blue than green light (Horecker 1943), it clearly provides a significant reduction in hemodynamic signals, especially around vasculature (Figure 3C). Future studies may improve on this correction method using measurements at multiple wavelengths to more accurately estimate the hemodynamic signal (Yoshida et al. 2015).

We note that this correction is not simply masking blood vessels, but preserves the underlying change in fluorescence, as seen in Figure 3F. Because regions with vessels are darker, they emit fewer photons which will result in higher shot noise and slightly lower SNR around vessels, although this was not apparent in resulting maps.

This visual stimulus resulted in evoked activity in posterior areas, corresponding to the known location of visual cortex (Figure 4A,B). The individual frames in Fig 4A, as well as Supplemental Movie 1, demonstrate that activation was clearly visible on individual cycles without averaging. Averaging across cycles allowed evoked activity to be isolated from ongoing endogenous activity (Figure 4B).

We compared the spatial distribution of visually evoked activity with two other modalities. Vibrissal stimulation evoked activity in lateral cortex (Figure 4C), the known location of primary barrel somatosensory cortex, as well as midline regions corresponding to vibrissal motor cortex. Spontaneous locomotion (Figure 4D) activated regions of motor cortex and limb sensory cortex, together with weaker activation in posterior visual areas consistent with previously described locomotion signals (Andermann et al. 2013; Keller et al. 2012; Saleem et al. 2013). Figure 4E shows maps from the three modalities overlaid.

Retinotopic mapping to identify cortical areas across subjects

To map retinotopy in visually responsive areas, we used the periodic encoding method employed in both human fMRI and mouse intrinsic signal imaging (Engel et al. 1997; Kalatsky and Stryker 2003). In this approach, a stimulus periodically sweeps across the display. Assuming eye movements are unrelated to stimulus location, the amplitude of the Fourier component of the activity time series for each pixel at the sweep frequency

represents how strongly activity at each cortical location depends on stimulus location, while the phase corresponds to the stimulus location in retinotopic space. Although we did not measure eye movements, the consistent maps we recorded suggest eye movements were substantially unrelated to the stimulus under these conditions.

In order to evoke stronger visual responses than the typical, luminance bar or checkerboard, we used a vertical or horizontal bar of the binary spatiotemporal broadband noise described above (Figure 5A inset and Supplemental Movie 2). The sweep (10sec period) elicited corresponding waves of activity across the visual cortex (Figure 5A, Supplemental movies 2, and 3). Separate bands moving across primary visual cortex and smaller patches corresponding to extrastriate areas are easily distinguished. Indeed, clear retinotopic responses could be observed in single trials with no averaging (Supplemental movie 2), although averaging over stimulus cycles removed background cortical activity to isolate the stimulus-locked signal (Figure 5A, Supplemental Movie 3).

Both the azimuth and elevation topographic noise stimuli elicited strong periodic responses, with fluorescence changes up to 25% (mean = 19.3+/-5.8% s.d., n=15 sessions in 5 mice). These resulted in clear topographic maps revealing a number of retinotopic areas with 5 minutes or less of imaging time (Figure 5B-D). Analyzing the correlation between maps obtained from shorter intervals of the data demonstrates that a single 10sec trial shows 85% correlation with the final map, and that one minute of data provides a nearly identical map (Figure 5B). Because the timecourse of the mapping stimulus (10sec) is slow relative to the GCaMP6s time constant, deconvolution did not have a large impact on the results, although it can be seen that the raw signal is slightly delayed due to temporal summation and the slow decay (Figure 5E).

In order to align maps across sessions and identify extrastriate areas across individuals, we computed the Jacobian (the concatenation of gradients in each direction) of retinotopic position, confirming that it is roughly constant within a given visual area, but unique across neighboring areas, as gradients are naturally sensitive to reversals. The Jacobian represents the progression of retinotopic position at each cortical location relative to neighboring cortex, while discarding differences in absolute positioning across sessions and individuals, eliminating error that would arise from attempting to align position directly.

The population we studied (male and female mice, age 2-8 months) was sufficiently uniform that rigid alignment by maximizing cross-correlation of the Jacobian yielded aligned topographic maps with an average pairwise correlation of 0.90 +/- 0.05 s.d. across 15 sessions in 5 mice. Averaging across sessions and subjects yields the pooled retinotopic maps shown (Figure 5F,G).

In order to define the boundaries of retinotopic areas, we used two approaches that both included the chirality of the azimuth and elevation maps, known as the visual field sign, developed by Sereno et al. (1994) and recently applied to mouse cortex by Garrett et al. (2014), discussed more fully in Methods. A watershed transform of retinotopic position, together with visual field sign boundaries, clearly isolates V1 plus 6 additional extrastriate areas (Figure 5H). The areas can also be directly visualized by mapping the visual field sign and one specific component of the Jacobian into RGB space (Figure 5I). Both methods generate a layout of extrastriate areas consistent with recent anatomical and functional studies (Garrett et al. 2014; Wang and Burkhalter 2007), including the visual field biases present in some regions such as the over-representation

of the medial visual field in RL and over-representation of lateral visual field in AM and PM (Garrett et al. 2014).

Imaging activity across cortex during a visual discrimination task

We next measured task-specific activity across these demarcated cortical areas while mice perform a visual discrimination task. We trained mice to indicate the orientation of a grating (horizontal or vertical) by moving a threshold distance either left or right on the spherical treadmill for water reward (Figure 6A). Mice initiated trials by remaining stationary for 1 second and were free to decide when to respond. Mice learned this task to high accuracy (>90%) in 3-4 weeks and performed hundreds of trials in each 1-2 hour session (mean = 245 +/- 90 s.d.). On typical trials, mice begin movement 0.25-0.35 secs after stimulus onset and cross threshold between 0.3-0.7 secs (Figure 6B). Accuracy was high within this window, whereas earlier and later responses drop to chance (Figure 6C). These tended to occur at the end of sessions (Figure 6D), presumably due to mice disengaging from the task structure during periods when they are too frantic, satiated, fatigued, or distracted. In human behavioral studies, trials with long reaction times also show poorer performance (Weissman et al. 2006).

Aligning the deconvolved neural activity signal to the stimulus onset reveals a progression of activity across cortical areas in the range of hundreds of milliseconds, during which the animal makes the perceptual judgment and performs the motor output to report a decision and receive the reward (Figure 7A,B). Average activation maps for three individual subjects show similar, though not identical, patterns of activity (Figure 7B). In order to align across subjects, behavior sessions included 5 minutes each of mapping stimuli along azimuth and elevation. By averaging all correct trials that crossed

response threshold between 0.4-0.6 sec, we observed the timecourse of activity in each cortical area (Figure 7C,D). The locus of early activity is in extratriate regions lateral to V1 that are proposed to be members of a "dorsal" stream homologous to that in primates (Wang et al. 2012).V1 is most active at intermediate times. In the last few hundred milliseconds, as expected during locomotor response, activity was strongest in the same area that was most active during spontaneous locomotion (Figure 4D) that likely includes hindlimb S1 (Fig 7C,D red). Notably, the same temporal pattern of activation was present in the raw data before deconvolution, although the dynamics are greatly broadened and less tightly locked to behavioral epochs, due to the relatively slow dynamics of GCaMP6s (Figure 7E).

Curiously, a small region between lateral extrastriate, barrel, and auditory cortex is active throughout the trial (Fig 7C arrow). The next section will return to this poorly understood area, which we refer to as area 39 based on Krieg (1946), although subsequent studies have assigned other designations. Lip and tongue representations in S1, which would presumably be activated by licking and reward consumption, are beyond the anterior lateral extent of the window.

Two-photon imaging of individual neuronal responses in behaviorally identified networks

Although the macroscopic scale examined up to this point provides a global network view of cortical processing, ultimately understanding the computations being performed requires access to activity in populations of individual neurons. Therefore, we conclude by examining the activity of individual neurons in area 39, the region identified at the macroscopic scale as active throughout the behavior.

First, to confirm that GCaMP6s expression in this mouse line does not disrupt response properties and that the expression is adequate for two-photon measurements at illumination levels low enough to avoid gross damage, we measured orientation selectivity in V1 neurons, which has been well-characterized in previous studies (Chen et al. 2013; Niell and Stryker 2008). Supplemental Movie 5 shows the robust V1 response to drifting square-wave gratings at two spatial frequencies (0.02 and 0.08cpd) and eight evenly-spaced orientations/directions of motion. Figure 8A shows baseline fluorescence of a typical field of view, confirming clear exclusion of GCaMP6s in nuclei in vivo. Figure 8B shows the pixel-wise responses, collapsing across both spatial frequencies and opposite directions of motion, showing a large fraction of cells with strong responses and high orientation selectivity. 75% of cells (357/479 cells; 3 mice) were responsive to this stimulus set, and 98% of responsive cells (349/357 cells; 3 mice) had an orientation selectivity index (OSI) greater than 0.33, corresponding to a 2:1 preference for optimal versus orthogonal stimuli. The median dF/F for responsive cells was 0.46+/-0.25 s.d (Figure 8C). The distribution of OSI across the responsive cells (Figure 8D) was similar to that measured previously in layer 2/3, both by electrophysiology (Niell and Stryker 2008) and two-photon imaging (Chen et al. 2013), although it is important to keep in mind that estimates of tuning curves with calcium imaging are susceptible to distortion due to nonlinearities of the indicator (Nauhaus et al. 2012). Notably, two-photon data were acquired using illumination intensities between 35-50mW at the specimen, a typical level for in vivo studies that does not cause significant cortical damage over multiple typical imaging sessions.

We next used widefield imaging to test whether we could elicit activity in area 39 in simpler contexts than the visual orientation discrimination task, and determine its precise location relative to other sensory cortices. Although the area was not strongly driven by visual or auditory input sufficient to drive other areas, it was highly active during spontaneous locomotion in mice trained on the orientation discrimination (Figure 9A), but not as clearly activated in untrained mice (data not shown). Without specific visual stimulation (dimly lit laboratory surroundings), two-photon imaging at the location targeted on vasculature (Figure 9B) revealed activity in many area 39 neurons to be either positively (45 +/- 6%) or negatively (18 +/- 5 %) correlated with spontaneous locomotion (Figure 9C,D,E,F; 284 cells; 3 mice, see methods for caveats on pooling data). This was in contrast to V1 where, consistent with previous studies (Andermann et al. 2013; Erisken et al. 2014), we found a much smaller fraction of cells modulated by running, 8 +/- 2% positively and 9+/- 2% negatively (489 cells in 3 mice). This also indicates that the strong correlations in area 39 were likely not due to motion artifacts coupled to locomotion.

These results establish a potential connection with the locomotor component of the discrimination task, which required the subject to first remain stationary to request a trial, and then locomote to indicate response. While additional functional properties of this region remain to be investigated, these data provide a direct demonstration of the capacity to identify cortical areas active during behavior and probe their properties at the cellular level.

Discussion

Widefield imaging of neural activity across cortex

The widefield imaging approach and transgenic GCaMP6s mouse line described here address the need for a high spatial and temporal resolution method to map the dynamics of neural activity across cortical areas during behavior. As we demonstrate, this enables the direct visualization of multiple regions involved in stages of a task, allowing identification and characterization of structures that might not be expected to be involved. Paired with subsequent two-photon imaging, this integrates studies of the temporal dynamics of brain function from the global level to local networks.

Previous studies have used intrinsic hemodynamic signals (Kalatsky and Stryker 2003; Schuett et al. 2002), metabolic autofluorescence (Andermann et al. 2011; Tohmi et al. 2014), or GCaMP3 (Issa et al. 2014; Marshel et al. 2011) to demarcate cortical regions based on sensory stimuli. However, these studies did not demonstrate the temporal resolution and sensitivity that are needed to analyze activity on the timescale of perception and behavior. Widefield imaging of voltage signals in mouse cortex, either with voltage-sensitive dyes or fluorescent proteins (Akemann et al. 2012; Ferezou et al. 2006; Mohajerani et al. 2013), has much higher temporal resolution than calcium imaging, but generally has smaller fractional changes with activity and has yet to be paired with controlled behavioral tasks.

The method we describe here tracks the dynamics of activity across functionally defined regions, with different areas showing distinct profiles of activation relative to the task (Figure 7). Importantly, we show that behavioral imaging data can be aligned with retinotopically mapped areas, and employ a quantitative method to assist in demarcation

of discrete extrastriate regions. Furthermore, this method extends to imaging over large regions of the dorsal surface of cortex, enabling study of the relation between multiple modalities (Figures 4 and 9A and see Glickfeld et al. (2014)).

Broad and robust expression of GCaMP6s using a transgenic mouse line

Imaging large brain areas simultaneously requires broad labeling with a fluorescent indicator. In contrast to viral transduction or *in utero* electroporation, both of which are limited to relatively local labeling, the extent of expression using a transgenic mouse line can be determined primarily by the selected driver line. Here we show strong expression in a high proportion of excitatory cortical neurons by using a CaMK2-tTA driver with a tetO-responsive GCaMP6s line. Furthermore, using viral delivery or electroporation can result in inconsistent targeting and expression levels, whereas expression in the transgenic line does not require an invasive step and is consistent within strain. Expression level is particularly important with genetically encoded calcium indicators, as expression that is too low prevents accurate measurements of activity, whereas expression that is too high is detrimental to the health of neurons (Tian et al. 2009). Fortunately, the level of expression in this line, when crossed to the CaMK2a-tTA driver, falls within the usable range for both widefield imaging and extended 2-photon imaging, without exhibiting the filled nuclei indicative of cellular toxicity. In addition, because transcription from the tetO promoter can be controlled by doxycycline, expression can be silenced until shortly before the experimental period. This may be particularly useful for driver lines active early in development, when high levels of an exogenous calcium buffer such as GCaMP6 might be deleterious, or if driver lines for other cell types result in unhealthy levels of expression.

Importantly, the imaging paradigm presented here should be broadly applicable to other GCaMP6 mouse lines that are developed, such as those that do not require a separate driver line (Dana et al. 2014) or those where expression is dependent on Cre recombinase (Madisen et al. 2015). In addition, because this line is driven by the tetO system, it provides an orthogonal targeting scheme to Cre control that may be useful for other imaging approaches.

In this study, although GCaMP6s was expressed in excitatory cells across cortical layers using a CaMK2-tTA driver, widefield signals likely originated mostly in layers 1 and 2/3, due to the high attenuation of blue light in tissue. In addition to neurons in these layers, processes from neurons in deeper layers together with projections from other cortical areas likely contribute to the activity observed. Also, although previous studies with GCaMP6 focus on action potential responses, it is possible that subthreshold calcium signals are present as well.

Driver lines that target more specific cell types could help isolate activity in particular populations. It will be especially interesting to determine the activation of different inhibitory cell types during behavior, where they may control the level of activation or synchrony based on behavioral state and task demands (Fu et al. 2014; Pi et al. 2013; Tiesinga et al. 2008). This imaging approach could also be applied with other optical measures of neural activity, such as voltage indicators, which might allow higher temporal resolution.

Imaging and analysis considerations

The signal-to-noise ratio provided by the combination of the ultra-sensitive GCaMP6s indicator, the sCMOS detector, and high numerical aperture lenses provided

high spatial resolution, sufficient to detect activity structure within extrastriate areas. The stimuli we used generated retinotopic maps with features as small as 50um. This was also the smallest observed scale of activity correlations during behavior. However, this is coarser than the spatial resolution measured by surface vasculature, presumably because widefield fluorescence imaging samples a large volume in depth outside of the focal plane.

The high signal-noise ratio also facilitates temporal deconvolution, which can be susceptible to noise. Although the decay time constant of the GCaMP6s response is roughly a half second, high frequency information is available in the faster rising edge, and deconvolution revealed activity changes at least as fast as our 100 ms imaging rate. Even faster imaging is possible, but high frequency information is ultimately swamped by shot noise and detector noise. Faster GCaMP6 variants exist, but have lower signal amplitude, so it remains to be determined whether deconvolution of signals from these indicators would net an improvement. In general, the large responses of the slower GCaMP6s used here may be preferable in many cases when measuring amplitude of responses over slower timescales (such as retinotopic mapping), whereas faster indicators may be preferable when the highest temporal resolution is essential.

Although deconvolution improves the interpretability of calcium imaging data in some respects, principally by reducing temporal summation and the long decay time, resulting in a potentially closer match to neural activity, it does have its own caveats. In particular, inaccurate fitting of the temporal response kernel can cause responses to shift forward in time excessively, although this is less likely due to the asymmetric nature of the measured kernel. Also, deconvolution assumes a linear response, which may result in

distortion of large signals and inaccurate summation of temporally overlapping signals such as sensory stimuli and motor outputs. Thus, although the deconvolved signal should generally be closer to neural activity, it will not be perfect and should be interpreted carefully.

One notable limitation to the widefield imaging approach is that not all cortical areas are readily accessible for imaging, even in a lissencephalic species such as the mouse. Those that are buried in the midline or require difficult surgical approaches may not be conducive to recording in alert animals. Systems involving prisms or endoscopes (Andermann et al. 2013; Ziv et al. 2013) may permit imaging of deeper structures, but would likely not allow the large field of view available on the dorsal surface

Imaging multiple visual areas during perception and behavior

The mouse has emerged as an important model system for visual function, as it shares many aspects of both local visual processing (Hubener 2003; Huberman and Niell 2011) and organization of higher visual areas (Glickfeld et al. 2014) with cats and primates including humans. Notably, in addition to primary visual cortex, there are at least 7 retinotopically mapped extrastriate visual areas in posterior mouse cortex, and both connectivity and functional properties suggest an organization into two streams analogous to the dorsal and ventral streams of primates (Andermann et al. 2011; Marshel et al. 2011; Wang et al. 2011). Although differential tuning for stimulus properties such as spatial and temporal frequency have been described, specific roles in visual behavior for each area remain to be determined.

Here we have demonstrated an integrated approach to studying the functional role of the constellation of cortical visual areas. We begin by mapping the visually responsive

regions with a high signal-to-noise ratio that allows us to align across sessions and across animals, which enabled differentiation of activity in identified extrastriate areas during visual behavior. New statistical methods for delineating retinotopic areas (Garrett et al. 2014) may benefit from the higher SNR provided by GCaMP6s imaging over intrinsic signal imaging, helping to solidify the demarcation of mouse extrastriate cortex. We also expect the higher SNR to allow efficient retinotopic mapping using non-periodic stimuli, thereby avoiding potential confounds due to spatiotemporal correlations in sweeping stimuli such as anticipation, adaptation, and pursuit-type eye movements.

For the orientation discrimination task presented here, our data reveal a distinct pattern of activation following stimulus onset, with an extrastriate region reaching its peak most rapidly, followed by V1 and another set of extrastriate areas, and finally somatosensory areas that are coupled to the locomotor response (Figure 7). The continuing rise in V1 response may be due to sustained visual input, locomotor signals, recurrent local activity, or top-down feedback from extrastriate and/or cognitive areas. On the other hand, the fast activation in extrastriate areas may also represent anticipatory potentiation, other task-specific signals (Cardoso et al. 2012), or activity in intracortical axonal projections into the region. We bear in mind that the dynamics of each cortical area may not be mutually comparable – even if initial activation progresses feed-forward from V1, rise-times and peak activations could differ simply due to differing internal network structure. This finding thereby opens up future studies of the intracortical circuits that determine the dynamics of neural activity specific to a perceptual task. It will also be informative to measure how activity profiles change over the course of training, beginning with naïve subjects.

In the final phase of this study, we used two-photon imaging to target networks of neurons in a functionally defined region. In this way, it is possible to bridge global dynamics down to ensembles of individual neurons within subject. Specifically, we measured the activity during locomotion in a parietal association area between visual, auditory, and somatosensory cortex. Interestingly, this area is adjacent to AL, which has been shown to respond to high speeds of visual motion as might be encountered during locomotion (Andermann et al. 2011), as well as to extrastriate visual areas that receive input via an extrageniculate pathway through lateral posterior nucleus of thalamus (Tohmi et al. 2014).

Krieg identified this region in rat as receiving projections from the three surrounding secondary sensory cortices, naming it “area 39” in homology with Brodmann's name for the inferior part of posterior parietal association cortex in primates, an area known for sensory integration that had been found to perform executive functions after lesions to premotor frontal cortex (Krieg 1947; 1946). Caviness confirmed the area was cytoarchitecturally distinct in mouse, but renamed it “area 2”, implying a predominantly somatosensory function and arguing that "it is doubtful that this cortical region of the rodent will prove to subserve complex functions comparable to those associated with field 39 in the primate brain" (Caviness 1975). Later studies in rats and mice support Krieg over Caviness, showing these higher-order regions between the primary sensory cortices to exhibit polymodal responses (Olcese et al. 2013), potentially co-registered feature maps (Brett-Green et al. 2003), connectivity with multiple sensory and executive areas (Hishida et al. 2014), recognition of stimuli as behaviorally significant (Geissler and Ehret 2004), and involvement in navigation and intentional

movements (Whitlock 2014). The activity we observed in this area may correspond with recognizing the behavioral relevance of the visual discriminandum and/or the correlated visual, somatosensory, and auditory sensations involved in the learned skills of controlling the treadmill and collecting the reward.

Beyond the demonstrated application to visual discrimination, we anticipate that the methods we describe will be broadly applicable to other sensorimotor and cognitive tasks. More generally, techniques such as this may enable linking features of brain-wide networks to those of cellular ensembles, which will likely be essential to understand the neural basis of perception and action.

Bridge to Chapter III

In this chapter, we describe methods for imaging neural activity at both mesoscale and two-photon resolution using a transgenic mouse expressing the fluorescent calcium indicator GCaMP6s. In Chapter III we use these methods to investigate changes in neural activity due to learning and task engagement.

Figure Legends

Figure 1. A transgenic GCaMP6s reporter mouse.

A) tetO construct used to generate transgenic mouse line. B) Isolated brain from GCaMP6s mouse crossed to CaMK2 driver, viewed under fluorescence dissecting scope, demonstrating strong expression restricted to cortex. Scalebar 5mm C) Low magnification coronal view, showing broad expression throughout cortex. Scalebar 2mm. D) High magnification coronal view, showing expression throughout the layers of cortex. Scalebar 500um. E) Confocal section showing that majority of neurons express GCaMP6s, with negligible filling of cell nuclei. Blue = DAPI counterstain. Scalebar 50um.

Figure 2. Widefield imaging of neural activity

A) Diagram of imaging and head-fixation setup. B) Widefield fluorescence image of GCaMP6s fluorescence in a cranial window. Inset shows positioning of cranial window. C) Fluorescence trace from a single 26um pixel, after blue-green subtraction, showing large step increases in fluorescence locked to timing of a 5sec on / 5 sec off noise stimulus. D) Cycle-averaged traces from the data in C, before (green) and after (black) temporal deconvolution, showing agreement with multi-unit electrophysiological recording (blue). Stimulus duration shown in grey.

Figure 3. Correction for hemodynamic signals.

A-C) Fourier phase maps in response to a 5sec on, 5sec off binary noise stimulus (as in Figure 2), showing significant vascular artifact present in green (A) and blue (B) illumination, but greatly reduced in the subtraction (C). D-F) Time course of signals for

point shown by circle in A-C, demonstrating that blue-green subtraction eliminates a delayed, slow dip evident in the green reflectance signal. Stimulus duration shown in gray.

Figure 4. Cortex-wide mapping of sensorimotor modalities.

A) Individual frames from two cycles (top and bottom rows) of a block-presentation visual noise stimulus, showing visually evoked activity superimposed on spontaneous activity. White arrowhead denotes location of visual cortex. B) Average response to presentation of visual noise stimulus. C) Average response to tactile whisker stimulation. D) Average activity during periods of locomotion. E) Overlay of responses during visual stimulus, whisker stimulus, and locomotion, demonstrating partitioning of cortex by functional properties. Average maps are based on 5 minute imaging sessions. Scalebar 2mm.

Figure 5. Mapping and alignment of retinotopically defined areas.

A) Individual frames from the cycle-averaged response to the topographic noise stimulus, showing that the moving stimulus evokes corresponding moving bands of neural activity in multiple cortical areas. See supplementary Movie 3 for full movie. B) Reliability of maps from short subsets of data, measured by correlation with map obtained from full 5 minutes of data C,D) Phase maps from one session in one mouse, demonstrating retinotopy in azimuth (C) and elevation (D). Color represents spatial position in degrees, based on phase of the Fourier response and the position and size of the monitor. Brightness represents Fourier amplitude. E) Timecourse for an individual pixel in (C) before and after deconvolution. F,G) Average retinotopic maps (azimuth and elevation, respectively) resulting from alignment across subjects and sessions, with correspondence

to known extrastriate areas based on demarcation in I. H) Overlay of visual field sign boundaries (black) with watershed transform of retinotopic location (gray) delineates known retinotopic regions. I) Color-coded map shows patches of consistent gradient and sign, representing discrete retinotopic regions. Assignment of cortical area identity in H, I and wireframe boundaries in I are based on previous anatomical and imaging studies. Putative assignment to processing streams, based on Wang et al. (2012) is shown in blue (ventral) and magenta (dorsal). F, G, H, I are averaged across 15 sessions in 5 mice. Scalebar in all panels is 500um.

Figure 6. Head-fixed visual discrimination task.

A) Schematic of head-fixed behavior paradigm, where mouse must run on the ball left or right depending on orientation of the stimulus. B) Distribution of response times from 15 sessions in 5 mice. C) Performance as a function of response time for sessions in B, showing high performance during an optimal response window. D) Median response time and percent correct through session duration, showing drop in performance toward the end of session.

Figure 7. Imaging spatiotemporal dynamics of cortical activity during a visual discrimination task.

A) Tracks of locomotor response during behavior for trials where the animal responded left versus right. Correct trials are labeled green, incorrect trials are labeled magenta. B) Average neural activity in individual subjects averaged across multiple imaging sessions, for trials when the animal responded between 400 and 600msec after stimulus onset, showing distinct patterns of activation across cortical areas at 100msec intervals. Each row represents an individual subject. C) Average neural activity aligned across 15

sessions in 5 subjects, with overlay of putative area boundaries from corresponding retinotopic mapping, showing temporally specific activation of restricted cortical areas that is consistent across subjects. Scalebar 1mm. D) Average timecourse at three cortical locations from data shown in C), at locations marked by colored squares in the right panel. Response is normalized to maximum for each location to demonstrate differences in temporal activation. Gray box shows response window.

Figure 8. Two-photon recording of passive visual responses in V1.

A) Baseline fluorescence image of a typical field of view in upper layer 2/3 of primary visual cortex. B) Pixel-wise map of orientation selectivity as measured with drifting gratings of two spatial frequencies and eight orientations, showing a large number of responsive cells with nearly all showing orientation selectivity. C) Histogram of visually-evoked dF/F for all cells recorded (n= 479 cells in 3 mice). D) Histogram of orientation selectivity for all visually responsive cells (n= 353 cells in 3 mice). Scale bar in A, B is 50um. Error bars represent bootstrapped confidence intervals.

Figure 9. Targeted two-photon recording in area 39 during spontaneous locomotion.

A) Overlaid widefield mapping of response to visual white noise stimulus. Scalebar 1mm. B) Widefield mapping of activity during spontaneous locomotion superimposed on an image of the vasculature, used to identify region for 2-photon recording. Scalebar 1mm. C) Pixel-wise correlation map between fluorescence traces and locomotion, showing neurons positively correlated with locomotion (red) and negatively correlated (blue). Scalebar 250um. D, E) Example fluorescence and locomotion traces from two neurons in C, showing activation correlated with locomotion (D) and activation correlated with stationary periods (E). F) Histogram of correlation between fluorescence

and locomotion for individual cells, with green representing cells that are significantly positively correlated and red representing cells that are significantly negatively correlated (n=284 cells in 3 animals).

Supplemental Movie Legends

Movie S1. Neural activity across multiple cortical regions during block presentation of a binary noise visual stimulus (upper left). In addition to clear stimulus-locked activation of visual areas, background activity in multiple areas is also evident. Movie is played at 4x actual speed.

Movie S2. Neural activity in visual areas during presentation of the topographic noise stimulus (upper left). The moving stimulus elicits moving waves of activity in multiple retinotopic visual areas, in addition to ongoing background activity. Movie is played at 4x actual speed.

Movie S3. Cycle-averaged activity during the topographic noise stimulus. Averaging over repeated presentations isolates stimulus-locked activity, showing multiple retinotopic areas. Movie is played at 4x actual speed, and repeats four times.

Movie S4. Timelapse movie of two-photon imaging in primary visual cortex, in response to drifting gratings, demonstrating large responses in a majority of neurons across a wide field of view. Movie is played at 4x actual speed.

Figures (Chapter II)

Figure 1

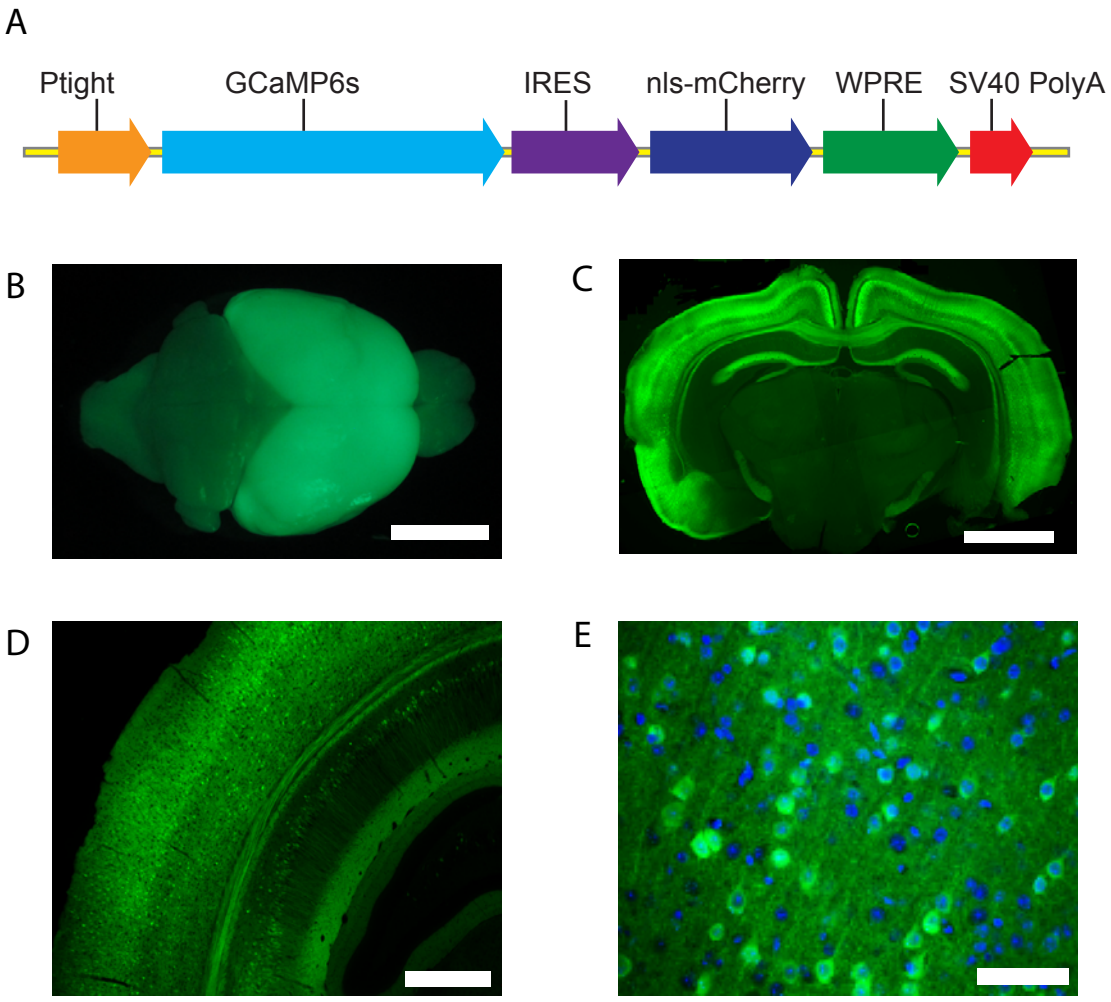

Figure 2

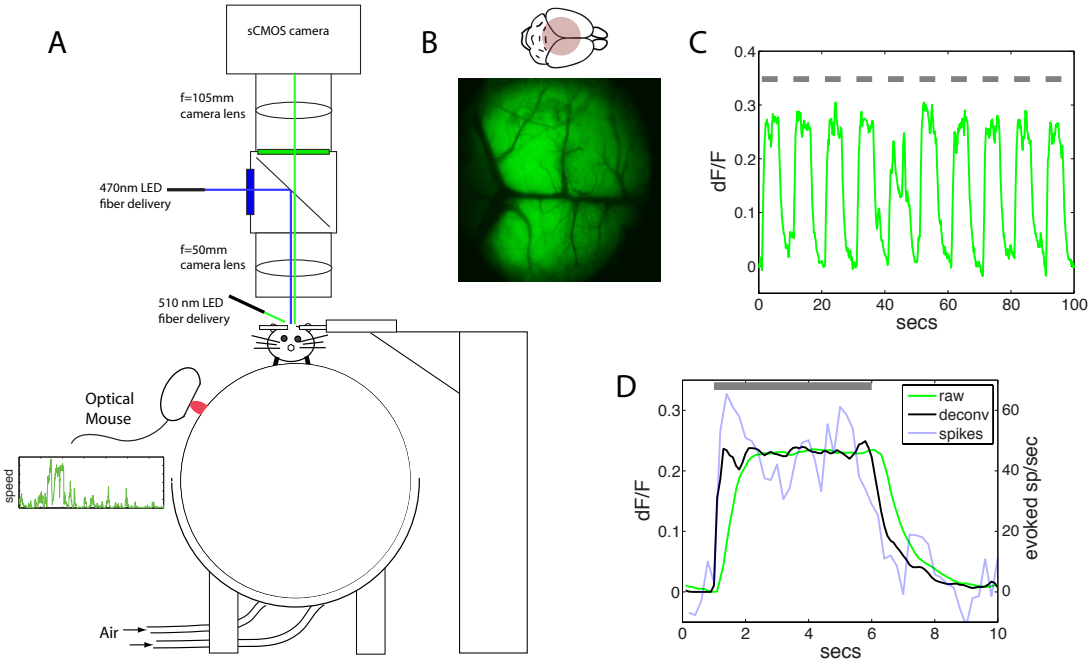
A
sCMOS camera
f=105mm
camera lens
470nm LED
fiber delivery
f=50mm
camera lens
510 nm LED
fiber delivery
Optical
Mouse
speed
Air
B
C
dF/F
secs
D
raw
deconv
spikes
dF/F
evoked sp/sec
secs

Figure 3

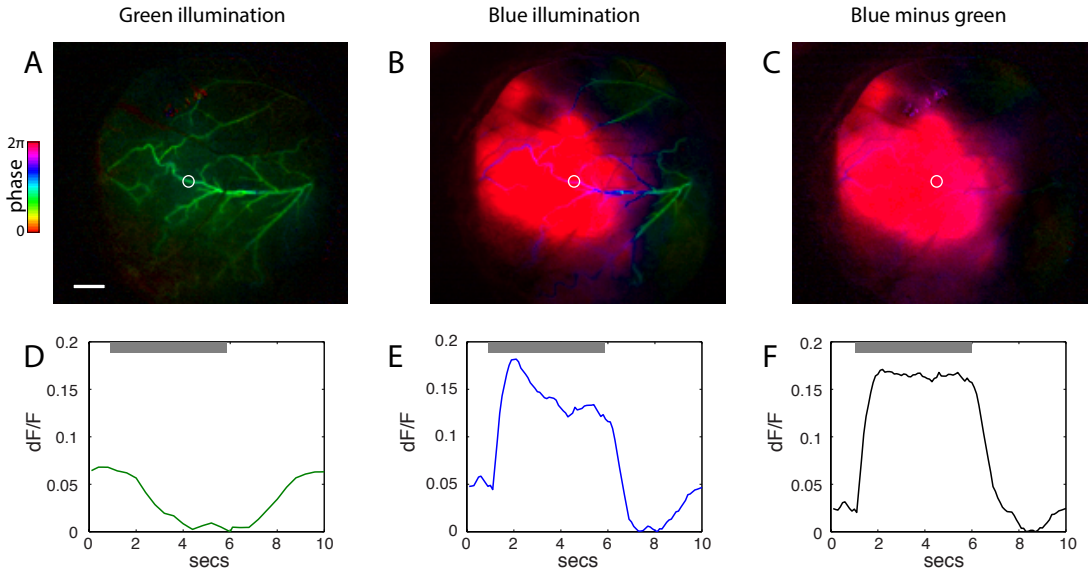
Green illumination
Blue illumination
Blue minus green
A
B
C
2π
phase
0
D
E
F
dF/F
0.2
0.15
0.1
0.05
0
0
2
4
6
8
10
secs

Figure 4

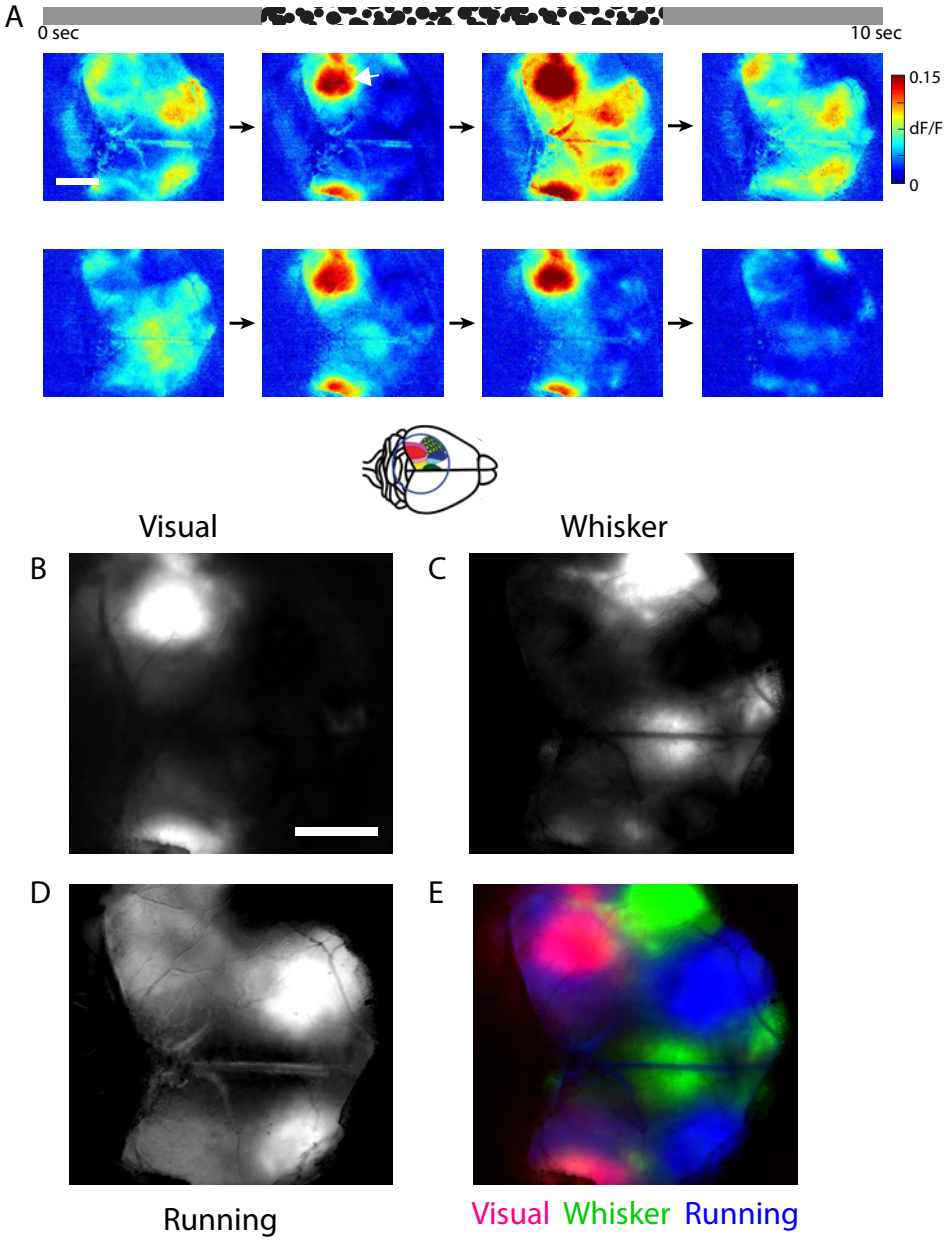
A
0 sec
10 sec
0.15
dF/F
0
Visual
Whisker
B
C
D
E
Running
Visual Whisker Running

Figure 5

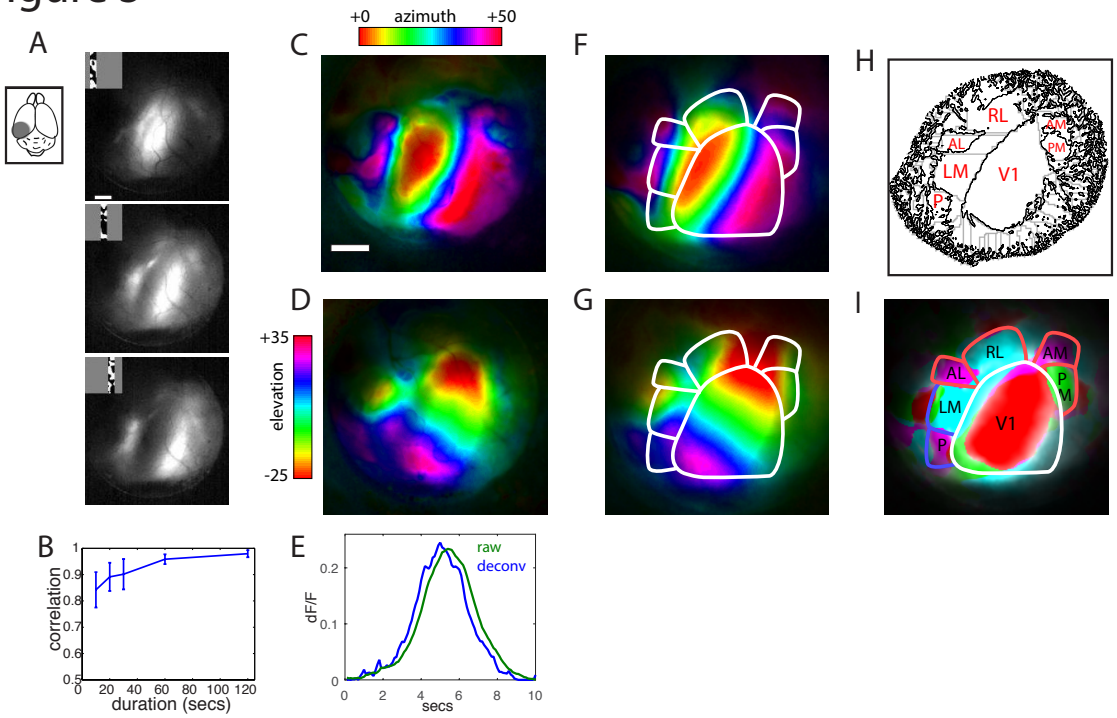
A
C
+0 azimuth +50
F
H
RL
AM
AL
PM
LM
V1
P
D
+35
elevation
-25
G
I
RL
AM
AL
P
M
LM
V1
P
B
correlation
1
0.9
0.8
0.7
0.6
0.5
0 20 40 60 80 100 120
duration (secs)
E
raw
deconv
dF/F
0.2
0.1
0
0 2 4 6 8 10
secs

Figure 6

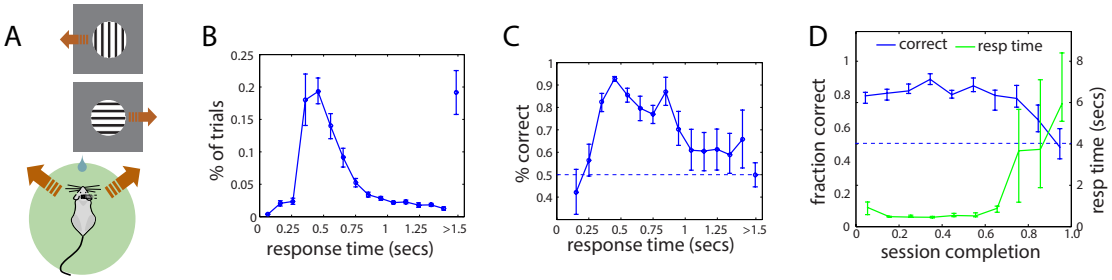
A
B
% of trials
response time (secs)
C
% correct
response time (secs)
D
correct
resp time
fraction correct
resp time (secs)
session completion

Figure 7

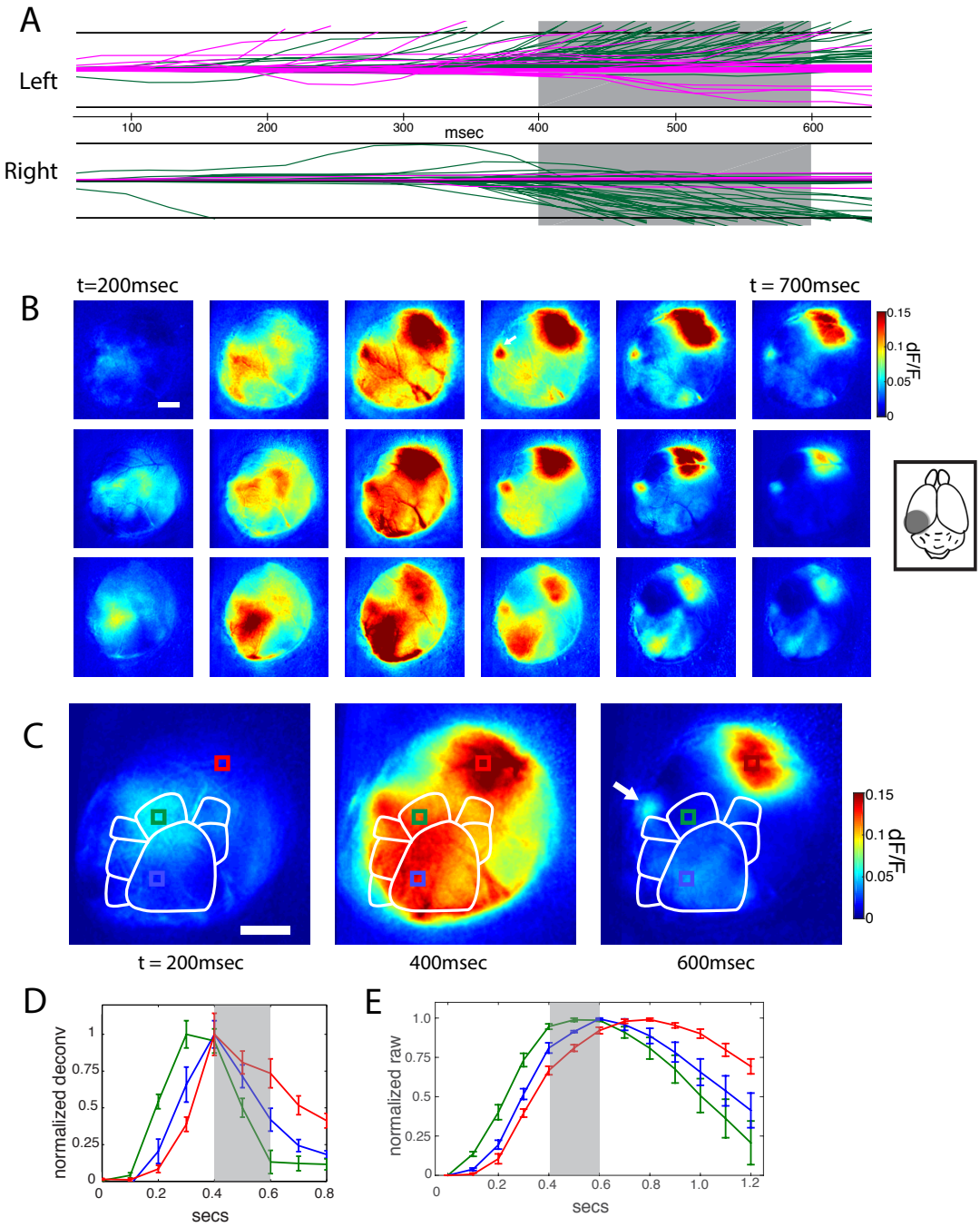
A
Left
Right
100
200
300
msec
400
500
600
B
t=200msec
t = 700msec
0.15
0.1
0.05
0
dF/F
C
0.15
0.1
0.05
0
dF/F
t = 200msec
400msec
600msec
D
normalized deconv
1
0.75
0.5
0.25
0
0
0.2
0.4
0.6
0.8
secs
E
normalized raw
1.0
0.75
0.5
0.25
0
0
0.2
0.4
0.6
0.8
1.0
1.2
secs

Figure 8

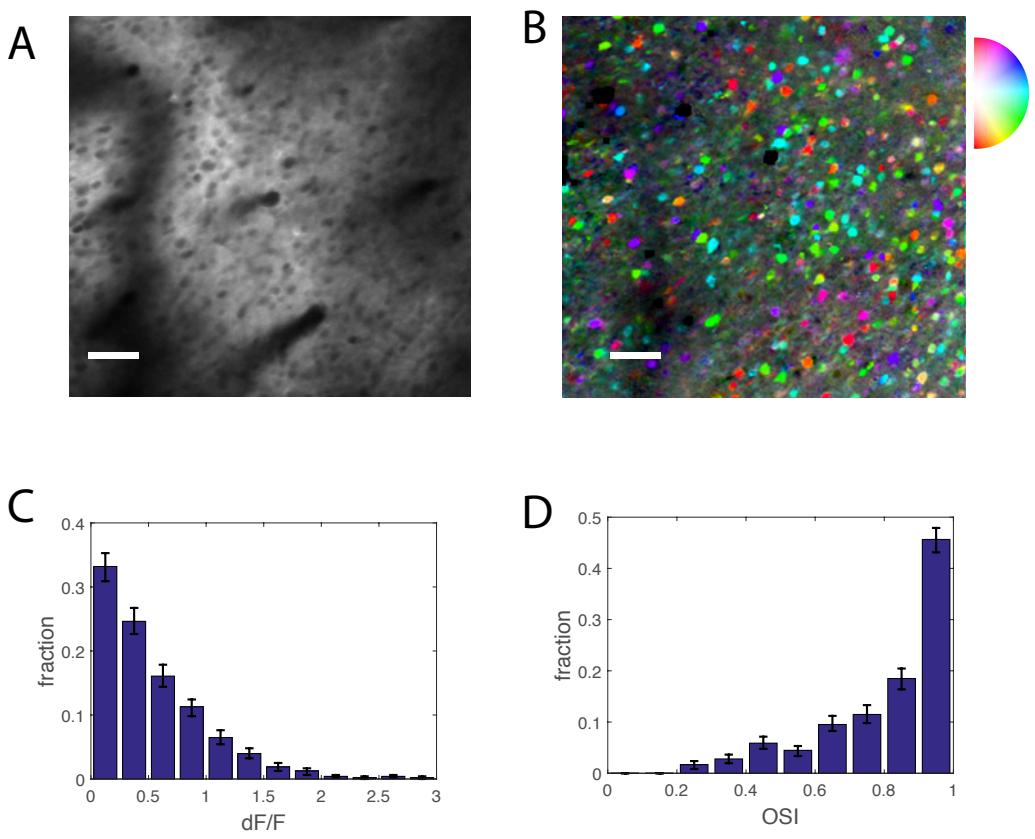

Figure 9

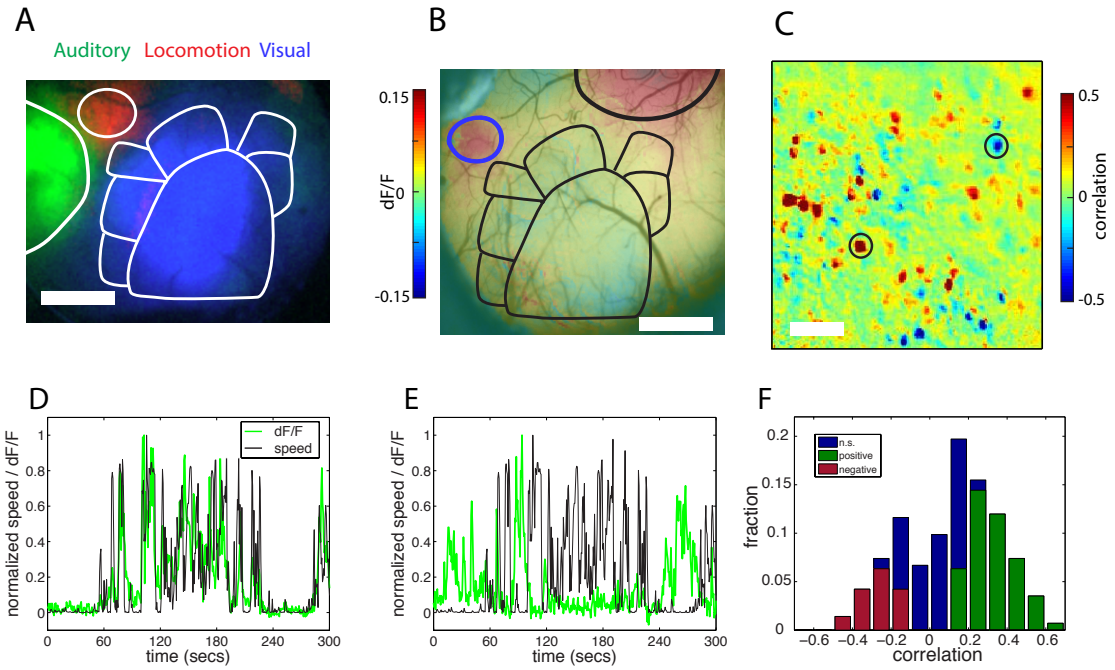
A
Auditory Locomotion Visual
B
0.15
dF/F
0
-0.15
C
0.5
0
correlation
-0.5
D
dF/F
speed
normalized speed / dF/F
time (secs)
E
normalized speed / dF/F
time (secs)
F
n.s.
positive
negative
fraction
correlation

CHAPTER III

DISTINCT FUNCTIONAL CLASSES OF EXCITATORY NEURONS ARE DIFFERENTIALL MODULATED BY LEARNING AND TASK ENGAGEMENT

This chapter includes unpublished co-authored material. Joseph B. Wekselblatt performed experiments; Joseph B. Wekselblatt and Cristopher M. Niell analyzed data; Joseph B. Wekselblatt and Cristopher M. Niell interpreted results of experiments; Joseph B. Wekselblatt prepared figures; Joseph B. Wekselblatt and Cristopher M. Niell wrote manuscript.

Introduction

Sensory perception is context dependent and has been shown to be modulated by task demands, learning and engagement. Specific task demands can modulate neural responses to improve the detection or discriminability of relevant stimulus features and spatial locations (Deubel, Schneider, & Paprotta, 1998; Poort et al., 2015; Slotnick, Schwarzbach, & Yantis, 2003). Likewise, learning can affect coding strategy leading to increasingly sparse (or robust) representations, changes in tuning, and shifts in excitatory/inhibitory balance (Chu, Li, & Komiyama, 2016; Peters, Chen, & Komiyama, 2014; Yizhar et al., 2011). Task engagement and arousal have also been associated with a multiplicative gain in response to relevant sensory stimuli reminiscent of studies showing that attention can enhance responses (McGinley, David, & McCormick, 2015; Niell & Stryker, 2010; Vinck, Batista-Brito, Knoblich, & Cardin, 2015; Wekselblatt & Niell, 2015).

However, the circuit mechanisms for context dependent processing of sensory information are poorly understood, especially among classes of excitatory neurons. Furthermore, it remains unclear which neural changes are related to improvements in behavior and which changes are associated with adaptation due to exposure. Recent studies have addressed the differences in the responses of inhibitory neuron subtypes (representing only 10-20% of cortical neurons) and their affects on learning (Kato, Gillet, & Isaacson, 2015; Kuchibhotla et al., 2016; Yavorska & Wehr, 2016), finding differential modulation of responses due to training in the three genetically distinct subtypes (Pv+, SOM, and VIP). It remains unclear, however, how much diversity there is in the excitatory population, which represents ~80% of the neurons in cortex, and how potential sub-populations of the excitatory pool might contribute to context dependent perception. It is an important distinction that inhibitory neurons primarily affect local processing, while excitatory neurons, especially those in layer 2/3, send long range projections to other brain areas, determining what information is transmitted downstream.

Here we investigate which neuronal response changes allow context dependent information processing necessary to improve behavior based on task demands. To address this aim, we ask: “How do learning and exposure change sensory responses of excitatory neurons?” and “What are the response changes specific to being engaged in a task (active vs passive), and how does this modulation change over learning?”

To answer these questions we employed 2-photon imaging in headfixed animals performing a visual discrimination task before or after learning, or after exposure to the stimuli without learning a discrimination rule. We also track responses to passively presented stimuli identical to those used in the visual discrimination task. Furthermore,

we present a method for clustering of behavioral responses based on temporal dynamics, rather than tuning properties, which reveals striking heterogeneity in the pyramidal cell population in cortex, and suggests changes over learning are more specific than previously described.

We characterize three functionally distinct cell classes found in V1 excitatory population responsive during behavior (Transient, Sustained, Suppressed), showing that the pyramidal population in layer 2/3 is functionally heterogeneous. We also show that these cell classes exhibit specific changes in responsiveness over the course of learning, and that modulation by task-engagement is cell-type specific and depends on learning history.

Results

A headfixed paradigm to investigate sensorimotor learning in mice

To determine the effects of sensorimotor learning on V1 processing, we compared mice trained on a visual discrimination (trained) with mice that hadn't learned it (naïve). Additionally, to test whether observed changes were due to learning or exposure, we imaged mice that had viewed the same stimuli over a similar number of sessions as the trained mice but did not learn a discrimination rule (experienced).

To separate the acquisition of task structure (initiating trials and response) from learning the visual discrimination itself, we first trained all mice on a simple shaping task, luminance detection. Once mice consistently performed >200 trials per session at over 90% performance (~1-2 weeks) they were assigned to one of the 3 experimental groups described above. Initial shaping allowed us to study mice that were adept at self-initiating

trials and responding in a 2-AFC visual discrimination, so that differences were due to learning and not differences in trial structure, such as a failure to initiate or respond.

We then trained mice to perform a spatial localization task, reporting whether a stimulus was on the top or bottom of the monitor (Figure 10A). Stimuli were square wave grating patches of either horizontal or vertical orientation (Figure 10B). Animals in the 'naïve' group were imaged during their initial exposures (<8) to the grating stimuli immediately following mastery of the shaping task. Animals assigned to the 'experienced' group were presented with the same grating stimuli, but the spatial location of the stimulus did not predict reward. For the 'experienced' group the rewarded response direction was random on each trial. This allowed us to expose the animals to the same visual stimuli as the 'trained' group, but without allowing learning of a specific discrimination rule. Animals in the 'experienced' group were given approximately the same amount of exposure to the grating stimuli as the 'trained' group before imaging occurred (1-2 months, >50 sessions, >10,000 trials). Animals assigned to the 'trained' group were rewarded for responding correctly based on the location of the grating. Animals became proficient at the spatial discrimination task in 2-4 weeks. We performed imaging of the 'trained' group only after animals performed >200 trials per session at over 80% correct. Due to their experience in the 2-AFC paradigm during shaping, 'naïve' mice were able to self initiate trials and respond using the track ball with approximately the same frequency and time-course as the other two training groups (Figure 11).

Optogenetic silencing of visual cortex disrupts performance in the spatial location task

To determine whether visual cortex was necessary for the performance of the spatial discrimination task, we performed optogenetic inactivation of visual cortex. For

this manipulation, we trained transgenic animals expressing Cre-dependent channelrhodopsin (ChR2) in parvalbumin positive (Pv+) interneurons. Prior studies have shown that application of blue light in Pv/ChR2 animals causes almost complete silencing of the excitatory population, by strongly activating inhibitory drive to pyramidal cells through the local GABAergic fast-spiking interneurons (Burgess et al., 2017; Lien & Scanziani, 2013)

After reaching criterion performance in the spatial location task, animals received blue light stimulation through a chronic cranial window on 20% of trials, starting at visual stimulus onset and lasting until behavioral response. Silencing was done either by illuminating the entire cranial window (which includes several extrastriate visual areas) or restricting illumination only to V1. We found that performance in the spatial discrimination task was diminished to chance levels on silencing trials for animals expressing ChR2, in both the entire window ($p=0.0039$) and V1 ($p=0.0017$) shutdowns. Performance was not affected for the control animals that were expressing only GCaMP6 (Figure 10C). Importantly, reaction time was unchanged for all groups, suggesting that this was not due to impairment of motor output (Figure 10D).

Widefield mapping of visual cortex and targeting of stimulus location

For imaging, we used transgenic mice expressing a genetically encoded calcium indicator, GCaMP6s, under control of the CAMK2a promoter. This results in GCaMP6s expression in the majority of excitatory neurons in cortex (Wekselblatt, Flister, Piscopo, & Niell, 2016). To target 2-photon imaging to the specific cortical locations within V1 that represent the behavioral stimulus positions, we performed widefield retinotopic mapping (Figure 12). By mapping both azimuth and elevation using periodic topographic

stimulus, we were able to generate maps of the preferred locations in visual space for the population activity of all the pixels within the cranial window (Figure 12A-C). This allowed us to determine the specific cortical locations within V1 that represent the behavioral stimulus positions, for each individual mouse, using an overlay of vasculature landmarks (Figure 12 A,D).

To further confirm that the field of view (~800um x 800um) in our 2-photon recordings was centered at one of the stimulus locations, we performed retinotopic mapping of azimuth and elevation again, at 2-photon level following each behavior imaging session. We used this additional mapping step to determine the location of each imaged cell on the retinotopic map (Figure 12 E,F). Furthermore, we used this data to select only cells whose receptive field locations fell well within the bounds of our behavioral grating stimulus for further analyses (Figure 12G). Although the grating stimulus was ~33° **in** diameter, only cells that fell within a 24° diameter were used in subsequent analyses; this conservative bound was set so that cells whose receptive fields centers spanned the border of the behavioral stimuli were not included. Due to the limitations of the field of view, only one stimulus location could be imaged per session. The imaged location was alternated between the retinotopic location in V1 representing the top and bottom stimulus positions on each session. We then combined the responses for the preferred stimulus position (Figure 13A).

Heterogeneity in layer 2/3 excitatory population

We next measured task-evoked activity in the functionally defined regions of primary visual cortex while mice performed the behavioral tasks described above. Recordings were made at various depths in layer 2/3 of V1 (100-200um). We could

observe the activity of hundreds of simultaneously imaged excitatory neurons, both during behavior and passive. Figure 13A shows the timecourse of activity of all recorded neurons (>10,000) within the retintopic location of the stimulus, for each of the 4 stimulus conditions during correct behavioral responses.

Because we had responses from an extremely large number of neurons, rather than averaging we used a clustering approach to preserve heterogeneity while still allowing population characterization. Hierarchical clustering of the response time-courses during the behavior revealed striking heterogeneity in the layer 2/3 pyramidal population. Three distinct response types were found among neurons activated during behavior, which we term “transient”, “sustained”, and “suppressed” (Figure 13B). Transient cells exhibited a large and brief response at onset of the behavioral stimulus that quickly decayed. Sustained responding cells showed a slower rise to peak and continued to be active until the offset of the visual stimulus. Suppressed cells had high baseline firing rates and were suppressed during the time that the visual stimulus was present. This method of classification, based on the time course of response rather than tuning properties or choice probability, revealed surprising functional diversity in the layer 2/3 excitatory population, which has not been previously described. We used these classifications, obtained during behavior, to group cells for subsequent analyses.

Different functional cell classes show distinct selectivity and state dependence

In each imaging session, the mice also passively viewed identical stimuli to those presented during behavior, but with 2 additional orientations. This served two purposes: it allowed us to asses the effects of task-engagement on V1 processing, and allowed us to measure orientation selectivity and preference of recorded neurons.

Passive viewing of static grating patches of 4 evenly spaced orientations (0, 45, 90, 135) revealed that the distribution of orientation selectivity varied significantly ($p<0.001$) across all cell classes (Figure 14A). Sustained and transient cells have relatively high orientation selectivity (0.55 +/- 0.01, and 0.48 +/- 0.01 respectively). In contrast, suppressed cells show very little orientation preference (0.28 +/- 0.01), as has been reported for suppressed-by-contrast cells in previous studies (Niell & Stryker, 2010; Tailby et al., 2007). This difference in selectivity provides further evidence that the different response profiles we observed during behavior may in fact be a feature of distinct sub-populations within the pool of excitatory neurons within layer 2/3.

Furthermore, these cell classes show differential modulation by behavioral state. Locomotion has been shown to have a gain effect on sensory responses in cortex and has been shown to be coupled to arousal (McGinley et al., 2015; Niell & Stryker, 2010; Reimer et al., 2014; Vinck et al., 2015). Suppressed cells showed a much higher level of modulation of baseline firing rate with locomotion than either the transient ($p<0.001$) or sustained ($p<0.001$) cell classes (Figure 14B). The difference in response dynamics during behavior, passive receptive field properties, and level of modulation by behavioral state demonstrates that there is significant heterogeneity in the layer 2/3 excitatory population in V1 labeled by the CamK2 promoter.

Training affects proportion of responsive cells

To investigate whether there were long term changes associated with learning or exposure, we compared the fraction of responsive neurons during behavior between the behavioral training groups (trained, naïve, and experienced). We found that the proportion of recorded cells that were responsive during behavior was decreased in

'trained' and 'experienced' animals relative to the 'naïve' group ($p<0.05$ and $p<0.01$ respectively). Next, we looked to see which cell types were contributing to the diminished responses in learned and experienced animals. Both the 'trained' and 'experienced' groups showed a decreased proportion of transient responding cells compared to the 'naïve' group (Figure 15), although this was only significant for the trained group ($p<0.05$). We did not observe a significant change in the number of sustained or suppressed by contrast cells between groups ($p=0.12$ and $p=0.44$ respectively). This dissociation suggests a cell-type specific effect of learning versus extended exposure, which has not been previously described.

Despite the changes observed in the proportions of active cells during behavior across training groups, we did not find evidence that the response magnitude or timecourse was different for any of the cell classes across groups (Figure 16). Of the cells that were active during the behavior, the peak amplitude (Figure 16D) and temporal dynamics of the response were nearly identical for all three cell-classes (Figure 16A-C). This is consistent with previous studies showing learning related changes primarily affect the fraction of responsive cells, but not the magnitude of the responses in active neurons (Chu et al., 2016; Makino & Komiyama, 2015).

Training condition affects active/passive modulation

Next we looked to see whether training condition had an affect on visually evoked responses to the behavioral grating stimuli when presented passively. To achieve this aim, we compared the activity evoked during passive viewing across learning conditions for each cell type. To control for the differences in the observed proportion of active cells among training groups, we restricted this analysis to cells that were active during

behavior. Animals in the 'experienced' group showed little or no difference in passive responses compared to 'naïve' animals. In contrast, animals in the 'trained' group showed decreased activity for both transient ($p<0.01$) and sustained ($p<0.01$) cell classes relative to naïve animals (Figure 16E-H). Although the peak activity differed for the 'trained' group in the passive conditions, we observed little to no change in time course between groups. This suggests learning condition has a specific effect on the strength of passive responses, not seen in the behavioral response.

To determine how learning affected the level of modulation due to task engagement, we next compared active and passive responses to the grating stimuli for each cell class within the individual training groups. We found that for all cell classes within all training groups, responses to the behavioral stimuli were significantly larger ($p<0.001$) than the responses to the passive viewing of the same stimuli (Figure 17A-C). This difference between active and passive responses was especially pronounced for the group of animals who had been trained on the spatial discrimination (Figure 17A). To quantify this observation, we calculated a task modulation index (task – passive) / (task + passive) for each cell class and training group. Figure 17D shows that animals trained in the spatial location task had significantly higher task modulation index for both transient and sustained cell classes compared to 'naïve' animals ($p<0.05$), whereas 'experienced' animals showed little or no difference. Thus, in addition to cell-type specific changes in the proportions of active cells with learning, we also observe changes in the modulation of responses due to task-engagement, depending on the specific learning condition.

Discussion

In this study we sought to determine how different excitatory neuron types are modulated by learning and context. We show that pyramidal cells in layer 2/3 can be characterized into three functionally distinct sub-populations: transient, sustained and suppressed. Furthermore, these cell classes exhibit different selectivity and modulation by behavioral state. We find that experience and learning reduce the fraction of cells responsive to visual stimuli used in the behavior task. The reduction in responsive cells is specific to the transient population in trained animals, while experienced animals show reductions in both the transient and sustained populations. We did not observe significant changes in the evoked response magnitude or time-course, of the active neurons during behavior across any of the training conditions. However, we find that trained animals show enhanced modulation due to task engagement compared with naïve animals in both transient and sustained cell classes.

Previous research has shown similar decreases in population activity after learning in both human and animal studies(Chu et al., 2016; Makino & Komiyama, 2015; Peters et al., 2014). This shift in the fraction of active neurons may be an effect of repeated exposures to the same stimuli over the course of thousands of trials, or may reflect a more general design principle of sensorimotor learning in which sensory cortex aims to achieve efficient coding (Makino, Hwang, Hedrick, & Komiyama, 2016). Primary visual cortex has an enormous amount of potential downstream targets including extrastriate cortex, posterior parietal cortex, retrosplineal cortex, striatum and amygdala. The reduction in the fraction of behaviorally responsive neurons over training may represent an early mechanism for gating information flow to the appropriate target areas

needed to execute the proper behavioral output. This is an intriguing idea given that cortico-cortical neurons in V1 have been shown to convey specific information matched to the preferences of the downstream recipient area (Glickfeld, Andermann, Bonin, & Reid, 2013; Glickfeld & Olsen, 2017). Additionally, the reduction in active neurons over training has been observed in several brain areas including auditory cortex, olfactory bulb, motor cortex and visual cortex suggesting a potentially shared mechanism across sensory systems (Chu et al., 2016; Kato et al., 2015; Makino & Komiyama, 2015; Otazu, Tai, Yang, & Zador, 2009; Peters et al., 2014)

Our study provides the first report of sub-divisions within the excitatory pyramidal population that are differentially effected by learning and context. This characterization is an important step in determining the specific mechanisms by which information flow is routed to the correct brain areas for action. Local inhibitory neurons are also likely involved in this learning related reduction of excitatory responses. In primary visual cortex somatostatin (SOM) interneurons have been implicated in gating top-down effects of task engagement (Makino & Komiyama, 2015), and in auditory cortex both SOM and PV interneurons have been shown to provide context dependent synaptic inhibition and have a role in perceptual learning (Kato et al., 2015; Kuchibhotla et al., 2016). While context-dependent changes in inhibitory activity primarily affect local processing, changes in the pyramidal cell population (especially in layer 2/3) will have affects on both local and long-range synaptic partners and could function to gate the information sent to downstream areas(Glickfeld et al., 2013; Glickfeld & Olsen, 2017). It will be important for future studies to determine how these excitatory cell classes are

connected with and affected by different interneuron sub-types and long-range projections to and from other brain areas.

It is important to note the 'experienced' group may not be completely learning free. Due to the structure of the task, it is likely that these animals adopt a detection strategy, rather than a discrimination strategy, learning to move the ball and lick for reward when the stimulus appears even though there is no predictive power in the content of the stimulus. This may contribute to the similarities we see with the learned animals, in terms of the reduction of responsive neurons during behavior. It also remains an open question whether the observed changes are task specific or a general mechanism of learning. Replication of our findings with similar and different task demands should be done to tease this apart.

We also note that because we didn't perform chronic imaging of the same cell populations, we can't say what changes occurred to individual neurons over learning. Although we report population differences rather than changes in the same cells over time, our results are consistent with previous longitudinal studies on learning (Chu, Li, & Komiyama, 2016; Kato, Gillet, & Isaacson, 2015; Makino & Komiyama, 2015). Future longitudinal studies should be done to investigate the time-course of the reduction of responsive neurons of various excitatory subtypes and their correlation with improvements in behavioral performance.

The key question that our results bring up is: what are these cell types? The excitatory population in cortex labeled by the CaMK2 promoter includes roughly 80% of the neurons in cortex (Mayford, Bach, & Kandel, 1996; Wekselblatt, Flister, Piscopo, & Niell, 2016). Here we show that this population is not homogenous and can be sub-

divided into at least three functionally distinct populations. These populations may represent parallel processing streams analogous to the dorsal and ventral streams identified in humans and primates which have distinct projection patterns to downstream areas, specialized for processing different information (Binkofski & Buxbaum, 2013; Deubel, Schneider, & Paprotta, 1998; Hillyard & Anllo-Vento, 1998; Wang, Sporns, & Burkhalter, 2012). The functional differences observed here might also be a product of different inputs to the identified cell classes, potentially originating from different retinal ganglion cell types (Solomon, White, & Martin, 2002; Tailby et al., 2007). This brings forth the need to further identify these cell types using molecular or genetic markers, projection patterns, or anatomical reconstruction to help determine their role in cortical circuits underlying learning and behavior.

Task-specific processing allows context dependent behavior by flexibility extracting the most important information and channeling it to the appropriate downstream targets. Increasingly sparse activity over the course of learning may act to efficiently transmit information to the appropriate higher order areas for optimal decoding, representing an initial stage of routing. Here we report that the cortical excitatory population is heterogeneous and that distinct functional cell classes are differentially affected by task learning. Our identification of separate processing channels within the excitatory population will allow future studies to explore the diversity of projection pathways that allow context dependent processing.

Materials and Methods

Animal use

Animals were maintained in the animal facility at University of Oregon and used in accordance with protocols approved by the University of Oregon Institutional Animal Care and Use Committee (IACUC). All procedures were conducted in accordance with the ethical guidelines of the National Institutes of Health. Adult mice 2–6 months old, both male and female, were used in this study. Animals were maintained on a 12hr light / 12hr dark reverse light cycle, with training and experiments performed during the dark phase of the cycle.

Mice used for imaging experiments were a cross of GCaMP6-s under the control of TRE (jax 024742 (Wekselblatt, Flister, Piscopo, & Niell, 2016)), and CAMK2-tTA (jax 007004 (Mayford, Bach, & Kandel, 1996)). For optogenetic silencing of visual cortex, we crossed mice expressing Cre-dependent ChR2 (jax 012569) and Pv-Cre (jax 008069).

Surgical Procedures

The headplate and cranial window implant procedures were performed as described in Wekselblatt et al. (2016), with the following minor modifications. Briefly, a titanium headplate was cemented to the skull to allow head fixation in an initial surgery. Following recovery from the headplate surgery, a 5mm diameter cranial window (No. 1 coverglass, Warner Instruments) was implanted over visual cortex (3mm lateral, 1.5mm anterior of Bregma). For the headplate procedure, the imaging well of the headplate was filled with a thin layer of clear dental acrylic to protect the skull, instead of sylgaurd used in the previous description. We found that dental acrylic provided greater protection, as

the sylgaurd plug would sometimes fall out or cause condensation to be trapped inside the headplate well. For the cranial window procedure, dexamethasone sodium phosphate (2 mg/kg subcutaneously) was administered ~24 hr prior to surgery and again ~2 hr prior to surgery to reduce brain edema. We found that giving two doses of dexamethasone, instead of the single dose previously described, had a much greater effect at reducing brain swelling caused by the craniotomy. Finally, mice were allowed to recover for at least 1 week before beginning habituation and training. For the first 3 days we provided post-surgical animals with wet food in a small dish on the floor of their cage and a high calorie nutrient supplement (Nutri-Cal, Vetoquinol). This prevented weight loss after surgery and helped animals recover quickly.

Imaging

Our custom macroscope, used for widefield imaging, was as described in Wekselblatt et al. (2016). This design was based on the tandem lens system used for intrinsic signal imaging (Kalatsky & Stryker, 2003; Ratzlaff & Grinvald, 1991). Briefly, two camera lenses (Nikon 50mm f/1.2 and Nikon 105mm f/1.8) were interfaced with a dichroic filter cube (Thorlabs). Blue light illumination was supplied in epifluorescence configuration through the filter cube housing. Green light was supplied directly through a fiber placed obliquely above the brain. Images were acquired at 10Hz with 4x spatial binning using Camware software (PCO Corporation), with frame acquisition and LED illumination triggered by TTL pulses from the stimulus presentation computer to synchronize with visual stimulus frames.

Two-photon imaging was performed using a resonant scanning two photon microscope optimized for in-vivo imaging (Neurolabware, Los Angeles, CA) coupled to

a Mai-Tai HP Ti-Sapphire pulsed laser tuned to 920nm, with a 16x/0.8NA objective (Nikon). Scanbox software (Dario Ringach / Neurolabware) in Matlab was used for data acquisition. Images were acquired at 10 fps and 796x796 pixels over a ~800x800um field of view, using 65-110mW illumination power as measured at the front aperture of the objective. All recordings were targeted to layer 2/3 of V1 (depth 100 – 200 microns).

Stimulus delivery and behavior control

Visual stimuli were presented on a Viewsonic VA2342 LCD monitor (28 x 50cm, linearized to correct for gamma (mean luminance 35cd/m^2), oriented tangentially 25 cm from the mouse's right eye in portrait configuration (except during the shaping task), covering ~60x90° of visual space. Stimuli were generated with custom software using the Psychtoolbox extension for Matlab (Brainard, 1997; Pelli, 1997).

The behavioral control system was as described in Wekselblatt et al. (2016). Movement of the mouse on the spherical treadmill was measured with an optical USB computer mouse positioned laterally on the polystyrene ball, acquired once per stimulus frame (60Hz) in Matlab. Visual stimuli for behavior consisted of 33° diameter circular patches of stationary square wave gratings at random spatial phase with spatial frequency 0.08cpd, oriented either horizontally or vertically. Gratings appeared at one of two locations on the screen, either top or bottom (centered at +/- 20° from center of monitor in elevation).

For retinotopic mapping, we binarized a 1/f noise stimulus described previously (C. M. Niell & Stryker, 2008; Wekselblatt et al., 2016) with spatial frequency corner of 0.05cpd and cutoff of 0.12cpd, and temporal frequency cutoff of 5Hz. This noise stimulus was masked to create a 20 degree wide bar that moved across the visual display with a 10

second period in either azimuth or elevation for 30 cycles. This stimulus was binarized to black/white instead of grayscale to increase contrast and generate edges.

Passive viewing stimuli consisted of static grating patches identical to those presented during behavior (33° diameter, 0.08cycle/degree), with an additional location in the center of the screen and 2 additional orientations (45 and 135 degrees). Passive sessions consisted of 20 repetitions per stimulus, presented for 1 second each with an inter stimulus interval of 1 second.

Behavioral training

The spherical treadmill and headfixation were as described in Wekselblatt et al. (2016). Briefly, a 200mm hollow polystyrene ball was placed inside 250mm polystyrene hemisphere (Graham Sweets Studios, Cardiff, UK) supplied with airflow through a tygon tube positioned at the bottom pole. This provided a rotating surface on which the mouse was able to freely move. The animal's head was fixed via a surgically attached headplate that could be screwed into a rigid crossbar above the floating ball. Headplates were manufactured from titanium by emachineshop.com. Designs are available upon request.

Prior to beginning behavior, mice were handled for several days until they were comfortable with the experimenter. Once water scheduling was begun, animals received water only during and immediately after head-fixed training on the ball. Training sessions increased in duration over the course of 1–2 weeks, from 30 minutes to 1 hour sessions, and occurred twice per day separated by ~3 hours.

All training was performed with a mostly automated system (Wekselblatt et al., 2016). First, mice learned the simple visual task of discriminating the location of a

luminance stimulus with the screen in landscape orientation. Initially, animals were required to request a trial by stopping spontaneous locomotion for 1 second to receive a water reward. Upon requesting a trial, a stimulus was presented with dark on either the nasal or lateral 2/3 of the screen, and light on the other 1/3. The animal was rewarded with a second water drop for moving right (left) on the ball if dark was on the nasal (lateral). When an animal could reliably request trials, the water reward for stopping to initiate trials was eliminated. This task took about 1-2 weeks to learn and established trial structure and attention to the visual stimulus.

Water rewards were calibrated by the experimenter to maintain consistent weights (>80% of baseline), corresponding to ~0.8 – 1.0 ml of water through the course of a session. Mice were trained 2 sessions per day, 7 days per week for 30 – 60 minutes per session, with a session ending when the subject stopped initiating trials or performance dropped.

Once a mouse could perform a significant number of trials and reached ~85% accuracy on the luminance task, they were graduated to one of three task conditions (naïve, experienced, or trained). These tasks followed a similar trial structure to the luminance task, but a circular grating patch (either horizontal or vertical) was presented on either the top or bottom of the screen. The stimulus remained on the screen for one second after correct responses. Incorrect responses triggered a 3.5sec timeout with potentially aversive flashing error stimulus and 50% probability of a correction trial, where the previous stimulus was repeated until answered correctly, to prevent perseverative errors and bias.

Animals who were in the ‘naïve’ group were imaged during their initial exposures (<8) to the grating stimuli immediately following mastery of the shaping task. ‘Naïve’ animals were randomly rewarded during imaging sessions to ensure that they stayed naïve to any rule. Animals who were assigned to the ‘experienced’ group were moved to the grating stimuli but the spatial location of the stimulus did not predicted reward. Instead, the rewarded direction of motion of the trackball was random on each trial. Animals in the experienced group were given roughly the same amount of experience with the grating stimuli as the ‘trained’ group before imaging occurred (1-2 months, >50 sessions, >10,000 trials). Animals who were assigned to the ‘trained’ group were moved to the grating stimuli (fig 1b), and rewarded based on the location of the grating. Animals became proficient at this task in 2-4 weeks. Imaging occurred only after animals performed >200 trials per session at over 80% correct.

The imaging behavioral configuration was identical to training, except the stimulus remained on the screen for 1.5 s even after incorrect responses, replacing the flashing error stimulus used during training, to avoid differences in visual input between correct and error trials. Additionally correction trials were removed during imaging sessions to ensure each trial was independent from the previous answer.

Optogenetic Silencing

To perform optogenetic silencing we activated GABAergic fast-spiking interneurons (Pv+) expressing channelrhodopsin (ChR2) by illumination with a blue LED (470nm) through a chronic cranial window (Burgess et al., 2017; Lien & Scanziani, 2013). The animals used for optogenetic silencing experiments were trained on the spatial discrimination task until they reached criterion performance (>80% correct, >200trials

per session). Experimental animals were double positive for cre-dependent ChR2 (jax 012569) and Pv/cre (jax 008069). Control animals were GCaMP expressing animals used in the imaging experiments. We provided light stimulation through a chronic cranial window on 20% of trials, starting at visual stimulus onset and lasting until behavioral response. We performed silencing by illuminating either the entire cranial window (which includes several extrastriate areas) or restricted illumination to V1 by covering the rest of the window with black sylgaurd (Poort et al., 2015). The light intensity level used was 0.45mw/mm^2.

Data analysis – widefield imaging

As in Wekselblatt et al. (2016), to analyze widefield images, 3:1 alternating blue and green frames were separately interpolated to produce a continuous image series at 10Hz.. The fractional fluorescence change relative to the mean over the recording period (dF/F) was calculated for each pixel in each channel. The green channel was subtracted from the blue channel to correct for hemodynamic signals, giving a corrected fractional fluorescence intensity dF/F

For periodic stimuli (Figure 2), we computed the amplitude and phase of the Fourier component of the dF/F signal at the stimulus frequency (0.1Hz). For each pixel, the Fourier phase at which the amplitude peaks represents the retinotopic position that elicited the greatest visual response from the neural population at that cortical location. Retinotopic maps generated from widefield imaging were then used to target 2-photon recordings to the cortical region within the cranial window representing the behavioral stimulus locations (either top or bottom) based on vasculature.

Data analysis – two-photon imaging

Two-photon image data was first spatially aligned, using phase correlation to estimate x-y translation (courtesy of D. Ringach). Cell body ROIs were extracted semi-automatically, including neuropil subtraction and temporal deconvolution (Pnevmatikakis et al., 2016). Fractional fluorescence change (dF/F) was calculated for each cell, for each stimulus set.

Periodic mapping was performed immediately after 2 photon behavioral sessions to confirm accurate targeting of the retinotopic location in V1 representing the stimulus location. To ensure we had estimates of the spatial receptive field centers for all cells, we calculated a smooth map of retinotopy based on the neuropil response. Next, we calculated the retinotopic positions of each individual neuron based on its position on the neuropil map. 2-photon retinotopic mapping data was then used to restrict analysis only to cells whose location in the retinotopic map overlapped with the locations of behavioral stimuli. Although the stimuli were 33° in diameter**,** only cells whose receptive field centers fell within a 24° diameter (‘centered’) were used for analysis.

Hierarchical Clustering was performed on the response time-courses of imaged ‘centered’ cells for rewarded trials using Wards criterion (matlab). Analyses of modulation due to locomotion, and orientation selectivity were performed on all active cells for each cluster, regardless of the training group. For analysis of group differences of each cell class across training conditions, cell responses were averaged by individual sessions, and then session averages were combined among like training groups.

Statistical tests on cell responses were performed using the Kruskal-Wallis test, a nonparametric version of a one-way ANOVA. Multiple comparisons were made using

Tukey's honestly significant difference procedure. Significance testing for the fraction of active cells was performed using a one-way ANOVA. Unless otherwise noted, summary statistics are presented as means, with error bars representing standard error of the mean.

Figure Legends

Figure 10. 2-AFC behavior

A) Schematic of 2-AFC visual behaviors. Head-fixed mice move the spherical treadmill a threshold distance right or left in response to stimuli presented on a monitor. B) Stimuli presented for visual behaviors. Square wave grating (0.08 cycles/degree) of horizontal or vertical orientation located at the top or bottom of monitor. C-D) Optogenetic Silencing of visual cortex. C) Performance on spatial discrimination task is dependent on visual cortex. Pv+/ChR2 animals with full window or V1 only shutdown perform worse during 'light on' trials (0.45mw/mm^2). D) Mean reaction time with and without shutdown.

Figure 11. Initial shaping allows animals to learn task structure while restricting visual discrimination learning to the trained group.

A,B) Mean trial initiation times (A) and response times (B) for each training category, showing that all learned the task structure equally well. C) Mean performance in visual discrimination behavior for each group. * = $p<0.05$, ** =$p<0.01$, n.s. = not significant.

Figure 12. Targeted imaging of stimulus location in primary visual cortex (V1)

A) Single photon illumination of GCaMP6-s expression in visual cortex through chronic cranial window. Inset shows location of 2-photon recoding shown in (D-F). Scale bar = 1mm, applies to (A-C). B-C) Widefield retinotopic mapping of azimuth (B) and elevation (C), to functionally target 2-photon recordings to stimulus location. Colors represent position on monitor that elicited the greatest activity from each cortical location. D) 2-photon field of view in layer 2/3 of V1 (800um x 800um). E-F) 2-photon retinotopic mapping allows precise targeting of stimulus location in azimuth (E) and elevation (F). G) Receptive field centers for cells recorded from a single session. Blue circles denote

stimulus locations (33 degree diameter). Inner red circles represent selection criteria (24 degree diameter) for 'centered' cells included in analysis. Green dots are included cells. Black dots are excluded cells. Inset at top right shows location of cranial window and orientation of animal for panels A-F

Figure 13.Hierarchical clustering of response time-course reveals striking heterogeneity in layer 2/3 of V1.

A) Average response (dF/F) of imaged neurons in response to each of the four stimuli used for behavior (correct trials only). Responses sorted according to cluster identity based on time-course (inactive, transient, sustained, suppressed). B) Average evoked response time-course for each functional cell class, determined by cluster identity. Average from trials at preferred location only, pooled across orientations. T=0 represents stimulus onset.

Figure 14. Distinct functional cell classes exhibit unique differences in state modulation and orientation selectivity.

A-D) Modulation of spontaneous activity by locomotor state $(S_{run} - S_{rest}) / (S_{run} + S_{rest})$. A) Distribution of modulation by running of spontaneous activity (S) for transient cells (A), sustained cells (B), and suppressed cells (C). D) Average running modulation for each functional cell class, showing suppressed cells show greatest modulation of spontaneous activity by running. E-G) Distribution of orientation selectivity (circular variance) for transient cells (E), sustained cells (F), and suppressed cells (G). H) Average orientation selectivity for cells of each functional class. *** = $p<0.001$, n.s. = not significant.

Figure 15. Visual learning and exposure result in a reduction of the fraction of active cells in layer 2/3 of V1.

Fraction of active cells during behavior for each functional cell class and each training condition. * = $p<0.05$, ** =$p<0.01$, n.s. = not significant.

Figure 16. Training differentially affects magnitude of behavior and passive response to identical stimuli.

A-C) Average time-course of evoked activity during behavior for transient cells (A), sustained cells (B), and suppressed cells (C) by training condition. D) Average response at 'peak' time point for each cell class and training group during behavior (transient peak = 200-300ms, sustained/suppressed peak = 800 –900ms). No difference in magnitude observed across conditions. E-G) Average response time-course for evoked activity during passive viewing for transient cells (E), sustained cells (F), and suppressed cells (G) by training condition. H) Average response at 'peak' time point for each cell class during passive viewing. * = $p<0.05$, ** =$p<0.01$, n.s. = not significant.

Figure 17. Training enhances modulation due to task engagement.

A-C) Task evoked responses are enhanced relative to passive responses to the same stimuli for all training groups and cell classes. Responses evoked to grating stimuli during behavior and passive viewing for trained group (A), experienced group (B), and naïve group (C). D) Task modulation is enhanced by learning. Trained animals show greater modulation for transient and sustained cell classes. Task Modulation Index = $(Resp_{task} – Resp_{pass}) / (Resp_{task} –+Resp_{pass})$. * = $p<0.05$, ** =$p<0.01$, ***=$p<0.001$, n.s. = not significant.

Figures (Chapter III)

Figure 10

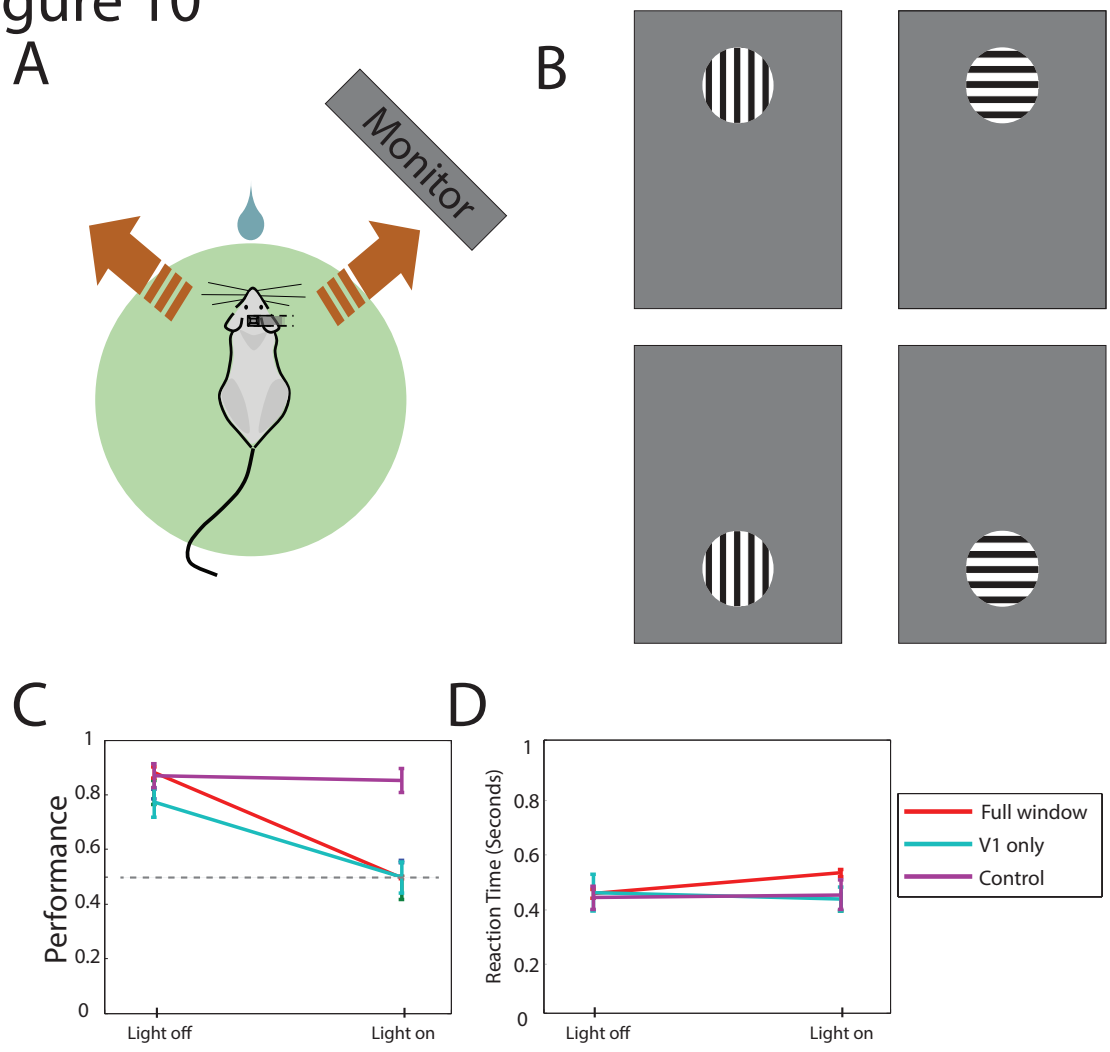

Figure 11

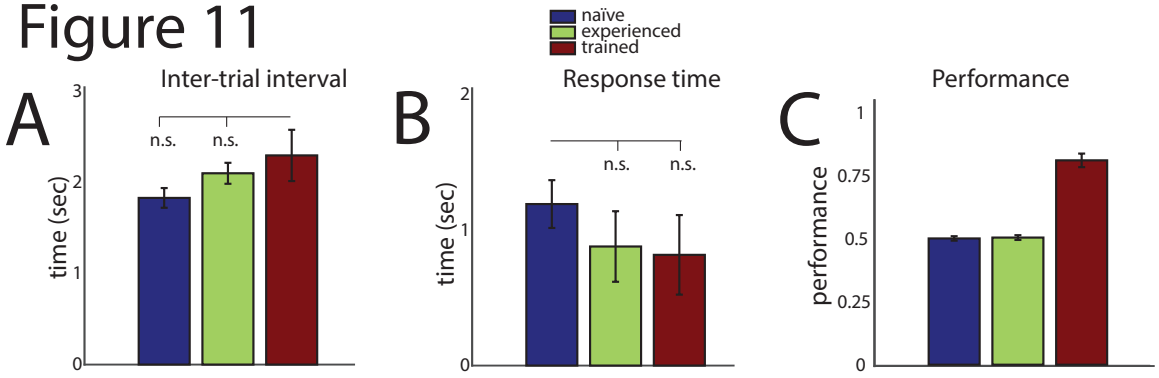
naïve
experienced
trained
A
Inter-trial interval
time (sec)
n.s.
n.s.
B
Response time
time (sec)
n.s.
n.s.
C
Performance
performance

Figue 12

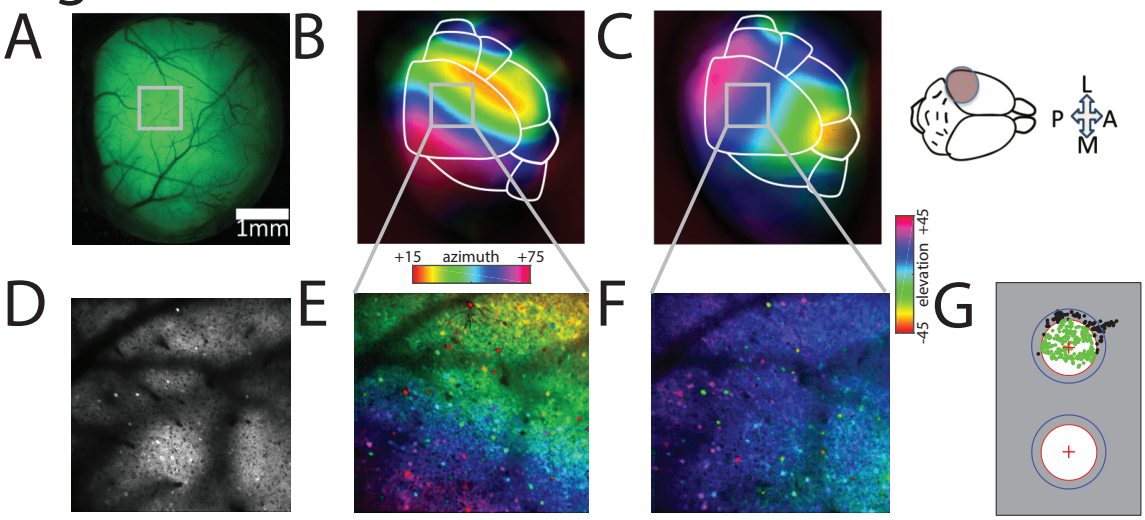

Figure 13

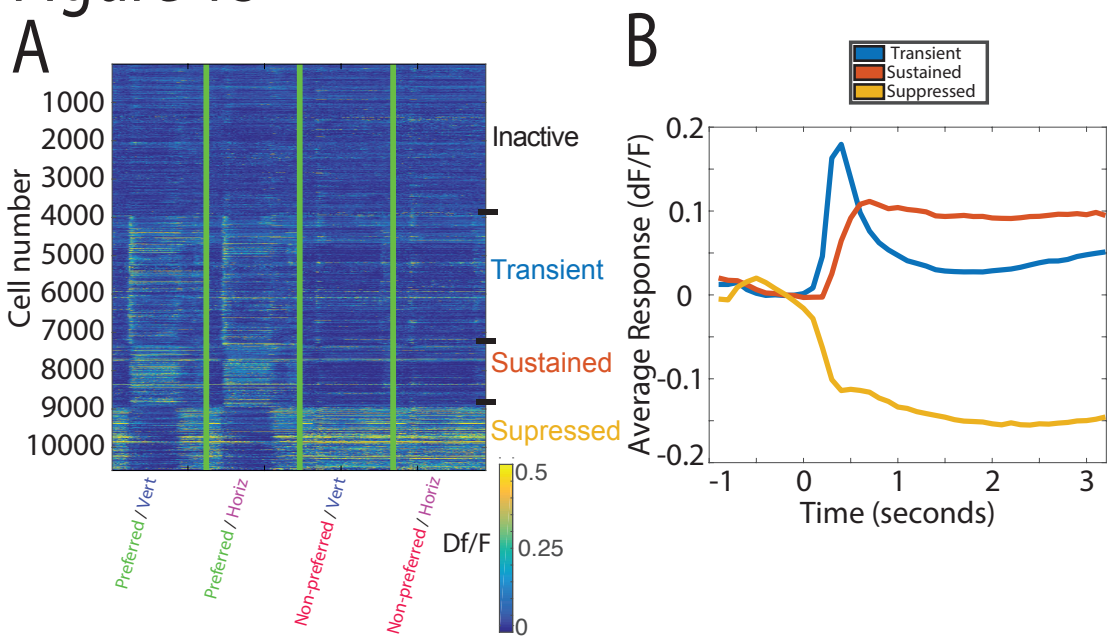
A
Cell number
1000
2000
3000
4000
5000
6000
7000
8000
9000
10000
Inactive
Transient
Sustained
Supressed
Preferred / Vert
Preferred / Horiz
Non-preferred / Vert
Non-preferred / Horiz
Df/F
0.5
0.25
0
B
Transient
Sustained
Suppressed
Average Response (dF/F)
0.2
0.1
0
-0.1
-0.2
-1
0
1
2
3
Time (seconds)

Figure 14

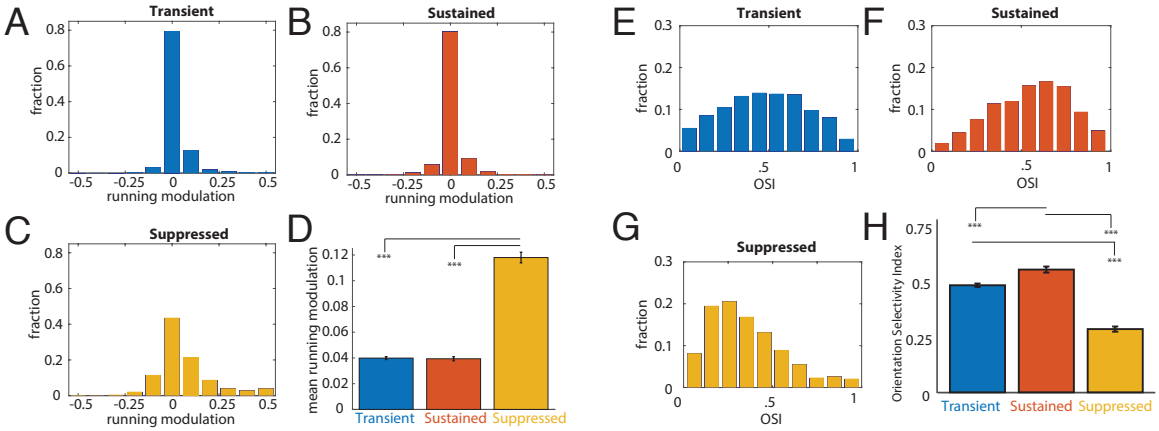
A
Transient
fraction
running modulation
B
Sustained
fraction
running modulation
C
Suppressed
fraction
running modulation
D
mean running modulation
***
***
Transient
Sustained
Suppressed
E
Transient
fraction
OSI
F
Sustained
fraction
OSI
G
Suppressed
fraction
OSI
H
Orientation Selectivity Index
***
***
***
Transient
Sustained
Suppressed

Figure 15

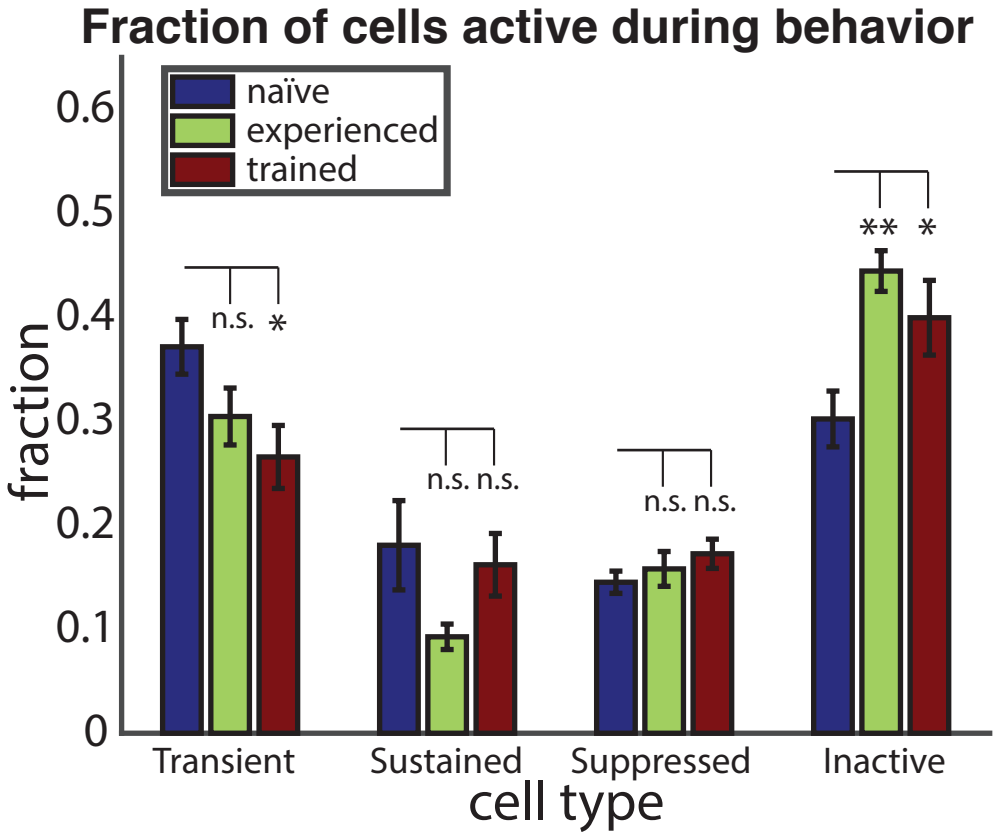
Fraction of cells active during behavior
naïve
experienced
trained
fraction
0.6
0.5
0.4
0.3
0.2
0.1
0
n.s. *
n.s. n.s.
n.s. n.s.
** *
Transient
Sustained
Suppressed
Inactive
cell type

Figure 16

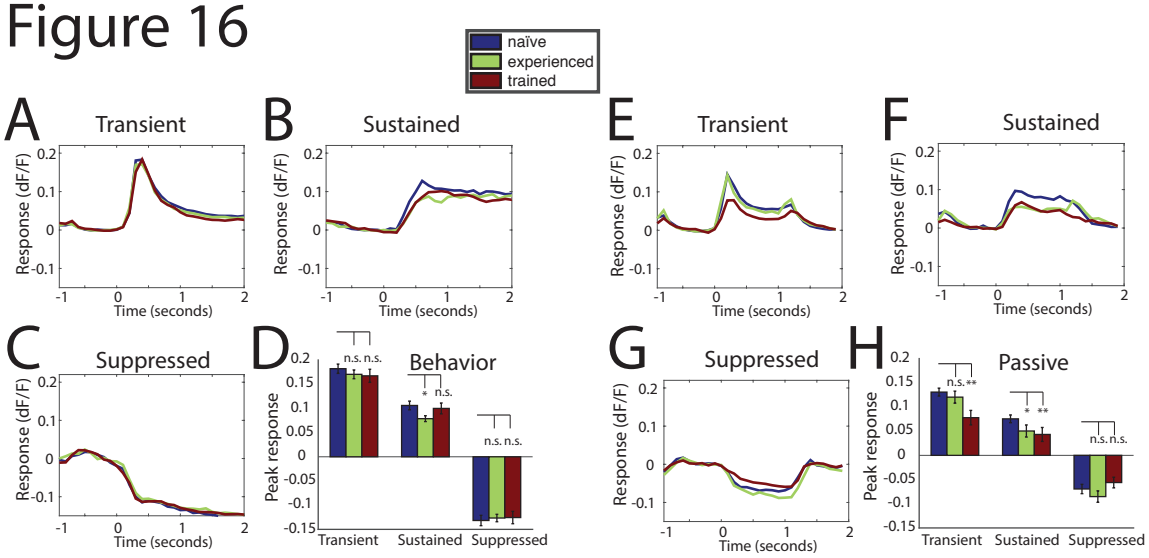
naïve
experienced
trained
A
Transient
B
Sustained
E
Transient
F
Sustained
C
Suppressed
D
Behavior
G
Suppressed
H
Passive
Response (dF/F)
Time (seconds)
Peak response
n.s.
*
**
Transient
Sustained
Suppressed

Figure17

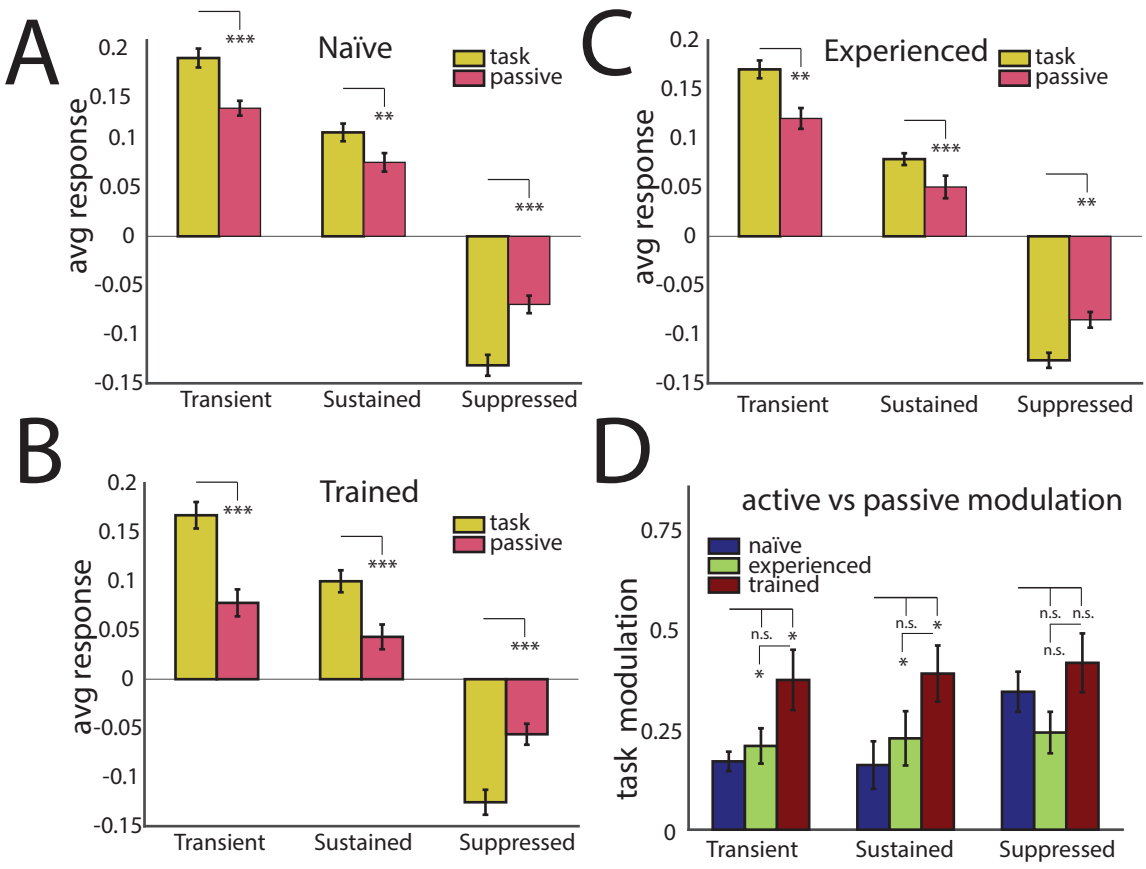
A
Naïve
task
passive
avg response
0.2
0.15
0.1
0.05
0
-0.05
-0.1
-0.15
***
**
***
Transient
Sustained
Suppressed
C
Experienced
task
passive
avg response
**
***
**
Transient
Sustained
Suppressed
B
Trained
task
passive
avg response
***
***
***
Transient
Sustained
Suppressed
D
active vs passive modulation
naïve
experienced
trained
task modulation
0.75
0.5
0.25
0
n.s.
*
*
n.s.
*
*
n.s.
n.s.
n.s.
Transient
Sustained
Suppressed

CHAPTER IV

CONCLUSIONS

This dissertation has focused on the interrogation of neural circuits involved in learning and behavior. In Chapter II we describe the creation of a new transgenic mouse, expressing a genetically encoded calcium indicator (GCaMP6s), and techniques for performing fluorescent calcium imaging at multiple spatial scales. Because sensory-driven behaviors engage many brain regions to process sensory input and generate motor output it is important to record activity over multiple spatial scales. The development of the tools and methods described here, combined with the implantation of a chronic cranial window and training of head-fixed visual discrimination behaviors has allowed us to probe the neural circuitry underlying context dependent sensory perception.

Through the implementation of widefield calcium imaging during behavior, we show the ability to identify patterns of activity that are associated with different phases of the visual discrimination task at high spatial and temporal resolution across a large portion of the animal's brain. We also show the ability to target specific areas that show conspicuous responses for two-photon imaging, and identify populations of individual neurons in one targeted region that correlate with locomotion in trained animals.

We then extend these techniques to investigate neural changes over learning, after observing a reduction in activity in mice that were trained in a visual discrimination behavior. To do this, we imaged mice before or after learning a visual discrimination, as well as a third group of animals that had been exposed to the stimuli in the context of behavior but were not able to learn a specific discrimination rule. Our results provide new

evidence of functional heterogeneity in the excitatory population of cortical layer 2/3 neurons and further suggest that there are cell-type specific changes in these populations due to both learning and task engagement

Using two-photon imaging in transgenic mice expressing the genetically encoded calcium indicator as described in chapter II, we were able to record from hundreds of neurons simultaneously while animals performed the visual discrimination behavior. Although imaging a large number of neurons simultaneously provides many advantages over conventional electrical recording techniques that are limited to a smaller number of neurons, analyzing massive numbers of responses presents significant challenges. This is especially true if the population of cells recorded is not homogenous. Advances in the molecular and genetic tools available to target recordings to genetically identified populations of neurons have helped restrict expression of indicators, however there is not a one-to-one mapping of gene expression to functional cell type. In the current study, we express the calcium indicator, GCaMP6-s, in cortical excitatory cells, however this population represents roughly 80% of the local neurons, likely representing several sub-populations. To address this challenge, we performed clustering on the time-course of responses to further delineate potential sub-groups of excitatory cells labeled by the CaMK2 promoter, which we identify as transient, sustained and suppressed groups.

We find that the functional cell classes identified by our clustering process exhibit different tuning and modulation by behavioral state, adding further evidence that these are distinct populations. We go on to show that training results in a decreases fraction of responsive neurons during behavior and that transient cells are specifically suppressed in learned animals. This shift in fraction of active neurons may be an effect of repeated

exposures to the same stimuli over the course of thousands of trials, or may reflect a more general design principle of sensorimotor learning in which sensory cortex aims to achieve metabolic efficiency. The increased number of responsive neurons in naïve animals could an initial expansion of the population encoding the stimuli early in training, and/or a process of later refinement often seen over the course of perceptual learning.

We also find that task engagement strongly modulates the responses of neurons in primary visual cortex. Animals from every training condition showed significantly larger responses in each of the functional cell classes during the behavioral condition compared to when passively viewing identical stimuli. We further quantified this difference by calculating a task modulation index, which compares the responses between active and passive conditions. We find that learning strongly affects the level of modulation due to task engagement, as animals that had learned the visual discrimination behavior showed increased modulation in both transient and sustained cell classes.

This work contributes important insight as to the cell types and task specific modulation underlying learning and behavior. We provide a new report of functional heterogeneity in layer 2/3 excitatory cells, which refines our understanding of the changes that occur over learning that enable context dependent sensory perception. Future studies should identify molecular or genetic markers to specifically label and manipulate the functional cell types described here to probe the anatomical and functional differences between them. These cells may receive different inputs and extend their processes to different downstream synaptic targets. The specific reduction in activity we see over learning may represent an early stage of information filtering that allows higher brain regions to more efficiently decode stimuli to make goal-directed decisions. If this is

the case, targeting these cell types for further investigation will be important for dissecting the contributions of different neural circuit elements to the parallel processing pathways that allow flexible behaviors in a complex sensory environment.

REFERENCES CITED

Chapter I

Burgess, C. P., Lak, A., Steinmetz, N. A., Zatka-haas, P., Harris, K. D., Burgess, C. P., … Carandini, M. (2017). High-Yield Methods for Accurate Two-Alternative Visual Psychophysics in Head-Fixed Mice. Cell Reports, 2513–2524.

Steinmetz, N. A., Buetfering, C., Lecoq, J., Lee, C. R., Peters, A. J., Jacobs, E. A. K., … Harris, K. D. (2017). Aberrant Cortical Activity in Multiple GCaMP6-Expressing Transgenic Mouse Lines. *Eneuro*, *4*(5), ENEURO.0207-17.2017.

Wekselblatt, J. B., Flister, E. D., Piscopo, D. M., & Niell, C. M. (2016). Large-scale imaging of cortical dynamics during sensory perception and behavior. *Journal of Neurophysiology*, *115*(6), 2852 LP-2866.

Chapter II

Ahrens MB, Li JM, Orger MB, Robson DN, Schier AF, Engert F, and Portugues R. Brain-wide neuronal dynamics during motor adaptation in zebrafish. Nature 485: 471-477, 2012.

Akemann W, Mutoh H, Perron A, Park YK, Iwamoto Y, and Knopfel T. Imaging neural circuit dynamics with a voltage-sensitive fluorescent protein. J Neurophysiol 108: 2323-2337, 2012.

Andermann ML, Gilfoy NB, Goldey GJ, Sachdev RN, Wolfel M, McCormick DA, Reid RC, and Levene MJ. Chronic cellular imaging of entire cortical columns in awake mice using microprisms. Neuron 80: 900-913, 2013.

Andermann ML, Kerlin AM, Roumis DK, Glickfeld LL, and Reid RC. Functional specialization of mouse higher visual cortical areas. Neuron 72: 1025-1039, 2011.

Benson DL, Isackson PJ, Gall CM, and Jones EG. Contrasting patterns in the localization of glutamic acid decarboxylase and Ca2+/calmodulin protein kinase gene expression in the rat central nervous system. Neuroscience 46: 825-849, 1992.

Brainard DH. The Psychophysics Toolbox. Spatial Vision 10: 433-436, 1997.

Brett-Green B, Fifková E, Larue DT, Winer JA, and Barth DS. A multisensory zone in rat parietotemporal cortex: Intra-and extracellular physiology and thalamocortical connections. J Comp Neurol 460: 223-237, 2003.

Carandini M, and Churchland AK. Probing perceptual decisions in rodents. Nat Neurosci 16: 824-831, 2013.

Cardoso MM, Sirotin YB, Lima B, Glushenkova E, and Das A. The neuroimaging signal is a linear sum of neurally distinct stimulus- and task-related components. Nat Neurosci 15: 1298-1306, 2012.

Caviness VS, Jr. Architectonic map of neocortex of the normal mouse. J Comp Neurol 164: 247-263, 1975.

Chen TW, Wardill TJ, Sun Y, Pulver SR, Renninger SL, Baohan A, Schreiter ER, Kerr RA, Orger MB, Jayaraman V, Looger LL, Svoboda K, and Kim DS. Ultrasensitive fluorescent proteins for imaging neuronal activity. Nature 499: 295-300, 2013.

Dana H, Chen TW, Hu A, Shields BC, Guo C, Looger LL, Kim DS, and Svoboda K. Thy1-GCaMP6 transgenic mice for neuronal population imaging in vivo. PLoS One 9: e108697, 2014.

Dombeck DA, Khabbaz AN, Collman F, Adelman TL, and Tank DW. Imaging large-scale neural activity with cellular resolution in awake, mobile mice. Neuron 56: 43-57, 2007.

Engel SA, Glover GH, and Wandell BA. Retinotopic organization in human visual cortex and the spatial precision of functional MRI. Cereb Cortex 7: 181-192, 1997.

Erisken S, Vaiceliunaite A, Jurjut O, Fiorini M, Katzner S, and Busse L. Effects of locomotion extend throughout the mouse early visual system. Curr Biol 24: 2899-2907, 2014.

Felleman DJ, and Van Essen DC. Distributed hierarchical processing in the primate cerebral cortex. Cereb Cortex 1: 1-47, 1991.

Ferezou I, Bolea S, and Petersen CC. Visualizing the cortical representation of whisker touch: voltage-sensitive dye imaging in freely moving mice. Neuron 50: 617-629, 2006.

Fu Y, Tucciarone JM, Espinosa JS, Sheng N, Darcy DP, Nicoll RA, Huang ZJ, and Stryker MP. A cortical circuit for gain control by behavioral state. Cell 156: 1139-1152, 2014.

Garrett ME, Nauhaus I, Marshel JH, and Callaway EM. Topography and areal organization of mouse visual cortex. J Neurosci 34: 12587-12600, 2014.

Geissler DB, and Ehret G. Auditory perception vs. recognition: representation of complex communication sounds in the mouse auditory cortical fields. Eur J Neurosci 19: 1027-1040, 2004.

Glickfeld LL, Reid RC, and Andermann ML. A mouse model of higher visual cortical function. Curr Opin Neurobiol 24: 28-33, 2014.

Hishida R, Kudoh M, and Shibuki K. Multimodal cortical sensory pathways revealed by sequential transcranial electrical stimulation in mice. Neuroscience research 87: 49-55, 2014.

Holtmaat A, Bonhoeffer T, Chow DK, Chuckowree J, De Paola V, Hofer SB, Hubener M, Keck T, Knott G, Lee WC, Mostany R, Mrsic-Flogel TD, Nedivi E, Portera-Cailliau C, Svoboda K, Trachtenberg JT, and Wilbrecht L. Long-term, high-resolution imaging in the mouse neocortex through a chronic cranial window. Nat Protoc 4: 1128-1144, 2009.

Horecker BL. The absorption spectra of hemoglobin and its derivatives in the visible and near infra-red regions. J Biol Chem 148: 173-183, 1943.

Hubener M. Mouse visual cortex. Curr Opin Neurobiol 13: 413-420, 2003.

Huberman AD, and Niell CM. What can mice tell us about how vision works? Trends Neurosci 34: 464-473, 2011.

Issa JB, Haeffele BD, Agarwal A, Bergles DE, Young ED, and Yue DT. Multiscale Optical Ca Imaging of Tonal Organization in Mouse Auditory Cortex. Neuron 2014.

Jackson N, and Muthuswamy J. Artificial dural sealant that allows multiple penetrations of implantable brain probes. J Neurosci Methods 171: 147-152, 2008.

Kalatsky VA, and Stryker MP. New paradigm for optical imaging: temporally encoded maps of intrinsic signal. Neuron 38: 529-545, 2003.

Keller GB, Bonhoeffer T, and Hubener M. Sensorimotor mismatch signals in primary visual cortex of the behaving mouse. Neuron 74: 809-815, 2012.

Krieg WJ. Connections of the cerebral cortex I. The albino rat. C. Extrinsic connections. J Comp Neurol 86: 267-394, 1947.

Krieg WJ. Connections of the cerebral cortex. I. The albino rat. B. Structure of the cortical areas. J Comp Neurol 84: 277-323, 1946.

Luo L, Callaway EM, and Svoboda K. Genetic dissection of neural circuits. Neuron 57: 634-660, 2008.

Madisen L, Garner AR, Shimaoka D, Chuong AS, Klapoetke NC, Li L, van der Bourg A, Niino Y, Egolf L, Monetti C, Gu H, Mills M, Cheng A, Tasic B, Nguyen TN, Sunkin SM, Benucci A, Nagy A, Miyawaki A, Helmchen F, Empson RM, Knopfel T, Boyden ES, Reid RC, Carandini M, and Zeng H. Transgenic mice for intersectional targeting of neural sensors and effectors with high specificity and performance. Neuron 85: 942-958, 2015.

Marshel JH, Garrett ME, Nauhaus I, and Callaway EM. Functional specialization of seven mouse visual cortical areas. Neuron 72: 1040-1054, 2011.

Mayford M, Bach ME, Huang YY, Wang L, Hawkins RD, and Kandel ER. Control of memory formation through regulated expression of a CaMKII transgene. Science 274: 1678-1683, 1996.

Meier P, Flister E, and Reinagel P. Collinear features impair visual detection by rats. J Vis 11: 2011.

Mohajerani MH, Chan AW, Mohsenvand M, LeDue J, Liu R, McVea DA, Boyd JD, Wang YT, Reimers M, and Murphy TH. Spontaneous cortical activity alternates between motifs defined by regional axonal projections. Nat Neurosci 16: 1426-1435, 2013.

Nauhaus I, Nielsen KJ, and Callaway EM. Nonlinearity of two-photon Ca2+ imaging yields distorted measurements of tuning for V1 neuronal populations. J Neurophysiol 107: 923-936, 2012.

Niell CM, and Stryker MP. Highly selective receptive fields in mouse visual cortex. J Neurosci 28: 7520-7536, 2008.

O'Connor DH, Huber D, and Svoboda K. Reverse engineering the mouse brain. Nature 461: 923-929, 2009.

Olcese U, Iurilli G, and Medini P. Cellular and synaptic architecture of multisensory integration in the mouse neocortex. Neuron 79: 579-593, 2013.

Pelli DG. The VideoToolbox software for visual psychophysics: transforming numbers into movies. Spatial Vision 10: 437-442, 1997.

Pi HJ, Hangya B, Kvitsiani D, Sanders JI, Huang ZJ, and Kepecs A. Cortical interneurons that specialize in disinhibitory control. Nature 503: 521-524, 2013.

Pologruto TA, Sabatini BL, and Svoboda K. ScanImage: flexible software for operating laser scanning microscopes. Biomedical engineering online 2: 13, 2003.

Prevedel R, Yoon YG, Hoffmann M, Pak N, Wetzstein G, Kato S, Schrodel T, Raskar R, Zimmer M, Boyden ES, and Vaziri A. Simultaneous whole-animal 3D imaging of neuronal activity using light-field microscopy. Nat Methods 11: 727-730, 2014.

Ratzlaff EH, and Grinvald A. A tandem-lens epifluorescence macroscope: hundred-fold brightness advantage for wide-field imaging. J Neurosci Methods 36: 127-137, 1991.

Saleem AB, Ayaz A, Jeffery KJ, Harris KD, and Carandini M. Integration of visual motion and locomotion in mouse visual cortex. Nat Neurosci 16: 1864-1869, 2013.

Schuett S, Bonhoeffer T, and Hubener M. Mapping retinotopic structure in mouse visual cortex with optical imaging. J Neurosci 22: 6549-6559, 2002.

Sereno MI, McDonald CT, and Allman JM. Analysis of retinotopic maps in extrastriate cortex. Cereb Cortex 4: 601-620, 1994.

Tian L, Hires SA, Mao T, Huber D, Chiappe ME, Chalasani SH, Petreanu L, Akerboom J, McKinney SA, Schreiter ER, Bargmann CI, Jayaraman V, Svoboda K, and Looger LL. Imaging neural activity in worms, flies and mice with improved GCaMP calcium indicators. Nat Methods 6: 875-881, 2009.

Tiesinga P, Fellous JM, and Sejnowski TJ. Regulation of spike timing in visual cortical circuits. Nature reviews Neuroscience 9: 97-107, 2008.

Tohmi M, Meguro R, Tsukano H, Hishida R, and Shibuki K. The extrageniculate visual pathway generates distinct response properties in the higher visual areas of mice. Curr Biol 24: 587-597, 2014.

Vogelstein JT, Watson BO, Packer AM, Yuste R, Jedynak B, and Paninski L. Spike inference from calcium imaging using sequential Monte Carlo methods. Biophys J 97: 636-655, 2009.

Wang Q, and Burkhalter A. Area map of mouse visual cortex. J Comp Neurol 502: 339-357, 2007.

Wang Q, Gao E, and Burkhalter A. Gateways of ventral and dorsal streams in mouse visual cortex. J Neurosci 31: 1905-1918, 2011.

Wang Q, Sporns O, and Burkhalter A. Network analysis of corticocortical connections reveals ventral and dorsal processing streams in mouse visual cortex. J Neurosci 32: 4386-4399, 2012.

Wehr M, Hostick U, Kyweriga M, Tan A, Weible AP, Wu H, Wu W, Callaway EM, and Kentros C. Transgenic silencing of neurons in the mammalian brain by expression of the allatostatin receptor (AlstR). J Neurophysiol 102: 2554-2562, 2009.

Weissman DH, Roberts KC, Visscher KM, and Woldorff MG. The neural bases of momentary lapses in attention. Nat Neurosci 9: 971-978, 2006.

Whitlock JR. Navigating actions through the rodent parietal cortex. Frontiers in human neuroscience 8: 2014.

Wiesenfeld Z, and Branchek T. Refractive state and visual acuity in the hooded rat. Vision Res 16: 823-827, 1976.

Yoshida K, Nishidate I, Ishizuka T, Kawauchi S, Sato S, and Sato M. Multispectral imaging of absorption and scattering properties of in vivo exposed rat brain using a digital red-green-blue camera. J Biomed Opt 20: 051026, 2015.

Ziv Y, Burns LD, Cocker ED, Hamel EO, Ghosh KK, Kitch LJ, El Gamal A, and Schnitzer MJ. Long-term dynamics of CA1 hippocampal place codes. Nat Neurosci 16: 264-266, 2013.

Chapter III

Binkofski, F., & Buxbaum, L. J. (2013). Two action systems in the human brain. Brain and Language, 127(2), 222–229.

Brainard, D. H. (1997). The Psychophysics Toolbox. Spatial Vision, 10(4), 433–436.

Burgess, C. P., Lak, A., Steinmetz, N. A., Zatka-haas, P., Harris, K. D., Burgess, C. P., … Carandini, M. (2017). High-Yield Methods for Accurate Two-Alternative Visual Psychophysics in Head-Fixed Mice Resource High-Yield Methods for Accurate Two-Alternative Visual Psychophysics in Head-Fixed Mice, 2513–2524.

Chu, M. W., Li, W. L., & Komiyama, T. (2016). Balancing the Robustness and Efficiency of Odor Representations during Learning. Neuron, 92(6), 1048–1061.

Deubel, H., Schneider, W. X., & Paprotta, I. (1998). Selective Dorsal and Ventral Processing: Evidence for a Common Attentional Mechanism in Reaching and Perception. Visual Cognition, 5(1–2), 81–107.

Glickfeld, L. L., Andermann, M. L., Bonin, V., & Reid, R. C. (2013). Cortico-cortical projections in mouse visual cortex are functionally target specific, 16(2).

Glickfeld, L. L., & Olsen, S. R. (2017). Higher-Order Areas of the Mouse Visual Cortex. Annual Review of Vision Science, 3(1), annurev-vision-102016-061331.

Hillyard, S., & Anllo-Vento, L. (1998). Event-related brain potentials in the study of visual selective attention. Proceedings of the National Academy of Sciences, 95(3), 781–787.

Kalatsky, V. A., & Stryker, M. P. (2003). New paradigm for optical imaging: Temporally encoded maps of intrinsic signal. Neuron, 38(4), 529–545.

Kato, H. K., Gillet, S. N., & Isaacson, J. S. (2015). Flexible Sensory Representations in Auditory Cortex Driven by Behavioral Relevance. Neuron, 88(5), 1027–1039.

Kuchibhotla, K. V, Gill, J. V, Lindsay, G. W., Papadoyannis, E. S., Field, R. E., Sten, T. A. H., … Froemke, R. C. (2016). Parallel processing by cortical inhibition enables context-dependent behavior. Nature Neuroscience, 20(October), 1–14.

Lien, A. D., & Scanziani, M. (2013). Tuned thalamic excitation is amplified by visual cortical circuits. Nature Neuroscience, 16(9), 1315–1323.

Makino, H., Hwang, E. J., Hedrick, N. G., & Komiyama, T. (2016). Circuit Mechanisms of Sensorimotor Learning. Neuron, 92(4), 705–721.

Makino, H., & Komiyama, T. (2015). Learning enhances the relative impact of top-down processing in the visual cortex. Nature Neuroscience, 18(8), 1116–1122.

Mayford, M., Bach, M. E., & Kandel, E. (1996). CaMKII function in the nervous system explored from a genetic perspective. Cold Spring Harbor Symposia on Quantitative Biology, 61, 219–224.

McGinley, M. J., David, S. V., & McCormick, D. A. (2015). Cortical Membrane Potential Signature of Optimal States for Sensory Signal Detection. Neuron, 87(1), 179–192.

Niell, C. M., & Stryker, M. P. (2008). Highly Selective Receptive Fields in Mouse Visual Cortex. Journal of Neuroscience, 28(30), 7520–7536.

Niell, C. M., & Stryker, M. P. (2010). Modulation of Visual Responses by Behavioral State in Mouse Visual Cortex. Neuron, 65(4), 472–479.

Otazu, G. H., Tai, L.-H., Yang, Y., & Zador, A. M. (2009). Engaging in an auditory task suppresses responses in auditory cortex. Nature Neuroscience, 12(5), 646–654.

Pelli, D. G. (1997). The VideoToolbox software for visual psychophysics: transforming numbers into movies. Spatial Vision, 10(4), 437–442.

Peters, A. J., Chen, S. X., & Komiyama, T. (2014). Emergence of reproducible spatiotemporal activity during motor learning. Nature, 510(7504), 263–7.

Pnevmatikakis, E. A., Soudry, D., Gao, Y., Machado, T. A., Merel, J., Pfau, D., … Paninski, L. (2016). Simultaneous Denoising, Deconvolution, and Demixing of Calcium Imaging Data. Neuron, 89(2), 299.

Poort, J., Khan, A. G., Pachitariu, M., Nemri, A., Orsolic, I., Krupic, J., … Hofer, S. B. (2015). Learning Enhances Sensory and Multiple Non-sensory Representations in Primary Visual Cortex. Neuron, 86(6), 1478–1490.

Ratzlaff, E. H., & Grinvald, A. (1991). A tandem-lens epifluorescence macroscope: Hundred-fold brightness advantage for wide-field imaging. Journal of Neuroscience Methods, 36(2–3), 127–137.

Reimer, J., Froudarakis, E., Cadwell, C. R., Yatsenko, D., Denfield, G. H., & Tolias, A. S. (2014). Pupil Fluctuations Track Fast Switching of Cortical States during Quiet Wakefulness. Neuron, 84(2), 355–362.

Slotnick, S. D., Schwarzbach, J., & Yantis, S. (2003). Attentional inhibition of visual processing in human striate and extrastriate cortex. NeuroImage, 19(4), 1602–1611.

Solomon, S. G., White, A. J. R., & Martin, P. R. (2002). Extraclassical receptive field properties of parvocellular, magnocellular, and koniocellular cells in the primate lateral geniculate nucleus. Journal of Neuroscience, 22(1), 338–49.

Tailby, C., Solomon, S. G., Dhruv, N. T., Majaj, N. J., Sokol, S. H., & Lennie, P. (2007). A New Code for Contrast in the Primate Visual Pathway. Journal of Neuroscience, 27(14), 3904–3909.

Vinck, M., Batista-Brito, R., Knoblich, U., & Cardin, J. A. (2015). Arousal and Locomotion Make Distinct Contributions to Cortical Activity Patterns and Visual Encoding. Neuron, 86(3), 740–754.

Wang, Q., Sporns, O., & Burkhalter, A. (2012). Network Analysis of Corticocortical Connections Reveals Ventral and Dorsal Processing Streams in Mouse Visual Cortex. Journal of Neuroscience, 32(13), 4386–4399.

Wekselblatt, J. B., Flister, E. D., Piscopo, D. M., & Niell, C. M. (2016). Large-scale imaging of cortical dynamics during sensory perception and behavior. Journal of Neurophysiology, jn.01056.2015.

Wekselblatt, J. B., & Niell, C. M. (2015). Behavioral State-Getting “In The Zone.” Neuron, 87(1), 7–9.

Yavorska, I., & Wehr, M. (2016). Somatostatin-Expressing Inhibitory Interneurons in Cortical Circuits. Frontiers in Neural Circuits, 10(September), 1–18.

Yizhar, O., Fenno, L. E., Prigge, M., Schneider, F., Davidson, T. J., O’Shea, D. J., … Deisseroth, K. (2011). Neocortical excitation/inhibition balance in information processing and social dysfunction. Nature, 477(7363), 171–178.